Astronomy & Astrophysics

Probing variability patterns of the Fe K line complex in bright nearby AGNs[⋆]

B. De Marco[1], K. Iwasawa[2], M. Cappi[3], M. Dadina[3], F. Tombesi[3,4,5,6], G. Ponti[7], A. Celotti[1], and G. Miniutti[8]

[1] SISSA International School for Advanced Studies, via Beirut 2-4, 34151 Trieste, Italy
    e-mail: demarco@sissa.it
[2] INAF – Osservatorio Astronomico di Bologna, via Ranzani 1, 40127 Bologna, Italy
[3] INAF – IASF Bologna, via Gobetti 101, 40129 Bologna, Italy
[4] Dipartimento di Astronomia, Università degli Studi di Bologna, via Ranzani 1, 40127 Bologna, Italy
[5] Department of Physics and Astronomy, Johns Hopkins University, 3400, Baltimore, MD 21218, USA
[6] Laboratory for High Energy Astrophysics, NASA/Goddard Space Flight Center, Greenbelt, MD 20771, USA
[7] APC Université Paris 7 Denis Diderot, 75205 Paris, France
[8] LAEX, Centro de Astrobiologia (CSIC–INTA); LAEFF, PO Box 78, 28691 Villanueva de la Cañada, Madrid, Spain

ABSTRACT

Context. The unprecedented sensitivity of current X-ray telescopes allows the issue of the Fe K line complex variability patterns in bright, nearby AGNs to be addressed for the first time. These kinds of studies have the potential to map the accretion flow in the strong gravity regime of supermassive black holes.
Aims. We examine XMM-*Newton* observations of the brightest sources of the FERO sample of radio–quiet type 1 AGNs (for a total of 72 observations) with the aim of characterizing the temporal behaviour of Fe K complex features.
Methods. A systematic mapping of residual flux above and below the continuum in the 4–9 keV range was performed in the time vs. energy domain, with the purpose of identifying interesting spectral features in the three energy bands: 5.4–6.1 keV, 6.1–6.8 keV, and 6.8–7.2 keV, respectively corresponding to the redshifted, rest-frame, and either blueshifted or highly ionized Fe Kα line bands. The variability significance of rest frame and energy-shifted Fe K lines was assessed by extracting light curves and comparing them with Monte Carlo simulations.
Results. The time-averaged profile of the Fe K complex revealed spectral complexity in several observations. Red- and blue- shifted components (either in emission or absorption) were observed in 30 out of 72 observations, with an average $\langle EW \rangle \sim 90$ eV for emission and $\langle EW \rangle \sim -30$ eV for absorption features. We detected significant line variability (with confidence levels ranging between 90% and 99.7%) within at least one of the above energy bands in 26 out of 72 observations on time scales of $\Delta t \sim 6$–30 ks. The reliability of these features has been carefully calculated using this sample and assessed at $\sim 3\sigma$ confidence level.
Conclusions. This work increases the currently scanty number of detections of variable, energy-shifted Fe lines and confirms the reliability of the claimed detections. We found that the distribution of detected features is peaked at high variability significances in the red- and blue- shifted energy bands rather than at rest-frame energies, suggesting an origin in a relativistically modified accretion flow.

Key words. line: profiles – relativity – galaxies: active – X-rays: galaxies

1. Introduction

Reflection features observed in the X-ray spectra of many active galactic nuclei (AGNs) represent a powerful tool for studying the properties of the matter flow accreting onto supermassive black holes (SMBH). In particular, the fluorescent Fe K line can be used to probe the innermost regions of AGNs (e.g. Fabian et al. 1989; Fabian et al. 2000; Reynolds & Nowak 2003; Miniutti & Fabian 2005), where the effects of general and special relativity become significant. Indeed, the relativistically skewed, red-shifted, and broadened profile of the line and its variability pattern strongly depend on the physical conditions of the accreting matter and of the SMBH (e.g its spin). By now about 25% of all AGNs observed by XMM-*Newton* appear to show a relativistic Fe line in their X-ray spectra (Guainazzi et al. 2006, hereafter

GBD06). Moreover, from a systematic study of 37 very high S/N, XMM-*Newton* observations of nearby ($z < 0.05$) radio quiet AGN, Nandra et al. (2007, hereafter NOGR07) demonstrate that Fe K line relativistic broadening is quite common, because effective in $\sim 45\%$ of the cases.

In recent years, more diversity has been added to the general picture by the discovery of narrow and (apparently) transient features in the $E \sim 4$–6 keV energy range (e.g. Turner et al. 2002; Longinotti et al. 2007a, and references therein; Vaughan & Uttley 2008), characterized by relatively short-time scale variability, of the order of tens of ks (e.g. Yaqoob et al. 2003; Iwasawa et al. 2004, hereafter IMF04; Tombesi et al. 2007, Petrucci et al. 2007). Their nature has not yet been understood. Vaughan & Uttley (2008) cast major doubts on the reliability of such shifted features, pointing out that many of the detections reported in the literature are not statistically significant and are most probably drawn from random fluctuations in the bulk of

---

[⋆] Figures 5–9, Tables 2, 3 and Appendix A are only available in electronic form at http://www.aanda.org

Table 1. Relevant features detected in the time-averaged spectra of the observations.

Source	Redshifted emission features	Broad Fe Kα	Highly Ionized Fe Kα/Fe Kβ	Absorption features
IC 4329a	670*		670*	670**
MCG -5-23-16	363**, 1099*		1099*	
NGC 3783	193**, 371**, 372*		193*, 371*, 372*	193*·**, 372*
NGC 3516	245*, 352*, 1250**	1251*		1250*, 1251*, 1252*, 1253*
MRK 509			250**, 1073**, 1074**, 1168*	1073**, 1168*·**
MCG -6-30-15	108A**, 302**, 303*	108A**, 301*, 303*	303**	108A*
MCG +8-11-11			794**	
NGC 7314			256*	
ARK 120		679*	679*	
MRK 279				1088**·*
NGC 3227	1279*			
IRAS 05078+1626			1410**	
MRK 590			837*	
MRK 766	265**, 999*, 1000**, 1001**, 1002**, 1003**	1000*, 1001*, 1003*, 1004**	82*, 265*, 999**, 1000**, 1001**, 1002*	
NGC 7469			912**	
MCG -2-58-22		180**		
NGC 526A			647*	647**
NGC 4051	263*, 541*		541**	263**
ESO 141-G055		1435A*, 1435B*, 1436*	1436**, 1445*	1445*
ESO 198-G024		207**		1128**
AKN 564		930*		
NGC 7213			269**	
NGC 4593			465*	

* Detection significance >4σ; ** detection significance between ∼3σ–4σ.

analysed X-ray data. As suggested by these authors, the detailed and deep investigation of a well-defined sample of objects, such as the one presented here, is necessary in order to come to a firm conclusion on this issue.

The importance of these features relies on their energy being similar to what is typical of relativistic Fe K line components, suggesting that we are observing the peak of a variable relativistic line profile produced in an extended region of the disk (in such a scenario, the red tail would be too faint to be detectable above the continuum). Alternatively, intrinsically narrow emission lines could be produced in discrete regions of inflows or outflows and redshifted as a consequence of relativistic motions. Moreover, recent results point towards an origin in small emitting regions within the inner accretion disk (e.g. IMF04, Tombesi et al. 2007; Petrucci et al. 2007), as predicted by several models, such as the "hot" orbiting spot model (Nayakshin & Kazanas 2001; Dovčiak et al. 2004) or the lamppost model (Martocchia & Matt 1996; Dabrowski & Lasenby 2001; Miniutti & Fabian 2004). Unfortunately, despite the unprecedented sensitivity of current X-ray telescopes, attempts to test these models are hampered by the too fine spectral features that are predicted (Goosmann et al. 2007). In this context, however, variability studies could be a key tool in providing insight into their real nature (e.g. Ponti et al. 2004; IMF04, Miller et al. 2006; Tombesi et al. 2007).

In this work we present the results from the time-resolved X-ray spectral analysis of a well-defined sample (94% complete) of radio-quiet AGNs from the XMM-*Newton* archive. The sample is a subset of the FERO sample (*Finding Extreme Relativistic Objects*) and was originally selected by GBD06 to study the general properties of relativistically broadened Fe Kα lines. We consider the same dataset with the aim of looking for transient features in the Fe K band and analyse their variability patterns by exploiting a uniform analysis of their highest quality observations. Several time-resolved studies have so far highlighted the variable nature of the Fe K line complex (e.g. Ponti et al. 2004; IMF04; De Marco et al. 2006; Miller et al. 2006; Petrucci et al. 2007; Tombesi et al. 2007). Up to now, there has, however, been no statistically solid characterization of its temporal behaviour. For the time-resolved analysis, we adopted the method based on mapping the excess residuals above and below the continuum

in the time vs energy plane, a technique that has been already widely used (Ballantyne et al. 2004, IMF04; Turner et al. 2006; Miller et al. 2006; Porquet et al. 2007; Tombesi et al. 2007; Petrucci et al. 2007) and has proven to be very useful for characterizing such variable X-ray spectral features.

2. Selection of the sample

The sample analysed in this paper was first presented in GBD06 and comprises 33 unabsorbed (namely with intrinsic N_H < $2–3 \times 10^{22}$ cm^{-2}), radio-quiet AGNs selected from the RXTE Slew Survey (XSS, Revnivtsev et al. 2004) to have $F_{2–10\,keV} \geq 1.5 \times 10^{-11}$ erg cm^{-2} s^{-1}. To carry out a meaningful timing analysis, all the XMM-*Newton* observations with EPIC pn exposure ≥10 ks were considered.

This selection excluded the following sources: H1846-786 (being observed two times for a duration of <10 ks) and UGC 10683 (because no XMM-*Newton* observations were available as of 2009 February 1). Furthermore, the source H0557-385 was discarded because its hard X-ray emission has been shown to be highly absorbed during the two ≥10 ks XMM-*Newton* observations. (The spectral curvature below 6 keV implies the presence of an intervening neutral gas cloud, partially covering the X-ray source, with a column density N_H ∼ 8×10^{23} cm^{-2} Longinotti et al. 2009.) Four observations (MCG-5-23-16, ID 0112830301; MRK 279, ID 0083960101; AKN 564, ID 0006810301; NGC 4593, ID 0109970101) were neglected after good time interval (GTI) filtering, as they result badly affected by proton flares, reducing the EPIC pn effective exposure to <10 ks. Finally a 15 ks observation of AKN 564 (ID 0006810101) was rejected as the effective exposure, although >10 ks is too short for the time resolution needed for the timing analysis. Our final sample consists of 30 sources and 72 observations. Information about the sample is given in Table 2.

In the following each observation is denoted by the corresponding XMM-*Newton* revolution number. Whenever more than one observation is carried out during the same revolution, a letter index indicates the chronological order.

3. Analysis

To characterize the variability pattern of the Fe K features using the so-called excess map technique (IMF04), it is important to identify a-priori the strongest lines in the spectrum. The first step is thus to define the properties of the average spectrum and then to analyse its temporal behaviour.

3.1. Data reduction and time-averaged spectral analysis

The analysis was carried out using only the EPIC pn camera data because of its higher sensitivity (about a factor of two, e.g. Watson et al. 2001) in the Fe K band, with respect to the EPIC MOS. We used the XMM-SAS v. 8.0.0 software with CCF release as of October 2006 for data reduction, and the *lheasoft* v. 6.0.3 package for data analysis. Time intervals free of high background events were selected by calculating the time-series average count rate μ and standard deviation σ_c during strong flare-free periods, in the $E \geq 10$ keV energy band and filtering out all the events with a count rate exceeding the (arbitrarily fixed) threshold of $\mu + 3\sigma_c$. This choice allows large data gaps to be avoided in the middle of the observation, which is a necessary condition for any timing analysis to be properly carried out. For each object, the source photons were extracted from a circular region of 45 arcsec radius, while the background ones were collected from adjacent source-free rectangular regions. Using the SAS task *epatplot*, we verified the presence of significant pile-up; whenever some degree of pile-up was found, it was minimized adopting an annular region for source counts extraction[1].

Average spectra were produced for each source and analysed using the XSPEC v. 11.2.3 software package. The spectral fitting was performed in the 4–9 keV energy band, where Fe spectral signatures are expected, using simple models (i.e. a power-law for the continuum and Gaussian components for emission and absorption lines). Some residual curvature of the spectrum produced by *warm absorber* systems can still be detected in this energy band. To correct the shape of the continuum for it, a cold absorption component was added to the model. (Clearly, the derived column densities, listed in Table 2, do not have any physical meaning.) It is worth noticing that the presence of narrow red- and blue- shifted absorption lines (Dadina et al. 2005; Reeves et al. 2004; Risaliti et al. 2005; Cappi 2006, and references therein; Braito et al. 2007; Tombesi et al. 2009; Cappi et al. 2009) in the chosen energy band did not significantly influence the determination of the continuum spectral shape.

We modelled emission and absorption lines in the time-averaged spectra with simple Gaussian templates. A Gaussian was added to the model whenever we found evidence of it from the 99% confidence contours for intensity vs energy. The best-fit models are reported in Table 3.

3.2. Results from time-averaged spectra

The "core" of the Fe Kα emission line is detected in all the observations (see Table 3). This line usually is relatively narrow with 1σ width of the order of the EPIC pn spectral resolution at these energies (i.e. ~0.13 keV) or less. A broader line at $E \sim 6.4$ keV ($\sigma \sim 0.2$–0.4 keV) is required in the spectral fitting

of NGC 3516 (rev. 1251), MCG -6-30-15 (rev. 108A, 301, 303), ARK 120 (rev. 679), MKN 766 (rev. 1000, 1001, 1003, 1004), MCG -2-58-22 (rev. 180), ESO 141-G055 (rev. 1435A, 1435B, 1436), ESO 198-G024 (rev. 201), and AKN 564 (rev. 930). The line energies are consistent overall with emission from neutral iron, although in some cases (NGC 3516 rev. 1251, 1253; MCG -6-30-15 (rev. 108A); MKN 766 rev. 999, 1003; ESO 141-G055 rev. 1435B; ESO 198-G024 rev. 207; AKN 564 rev. 930) the implied energies might be indicative of mildly ionized matter ($E \geq 6.45$ keV) or more complex line profiles.

Emission and/or absorption features at red- and blue- shifted energies were observed in 30 out of 72 observations. We detected significant redshifted emission in 21 out of 72 observations, with a 1σ width in the range <0.7 keV and $\langle EW \rangle \sim 90$ eV. It must be stressed that this is to be considered as a conservative number of detections because transient redshifted features might be smoothed out in the time-averaged spectra analysis, and hence not significantly detectable. Time-resolved surveys are the most suitable techniques for the study of this kind of feature.

Signatures of significant absorption lines blueward of the narrow "core" were instead detected in 15 out of 72 observations, at energies in the range $E \sim 6.6$–8.5 keV, with $\langle EW \rangle \sim -30$ eV.

Finally, lines consistent with emission from highly ionized Fe Kα and/or Fe Kβ were revealed in 28 out of 72 observations. The 1σ width of these lines were overall of the order of the energy resolution of the detector except for 12 observations (MRK 509 rev. 250, 1168; IRAS 05078+1626 rev. 1410; MKN 766 rev. 82, 265, 999, 1001, 1002; NGC 526A rev. 647; NGC 4051 rev. 541; ESO 141-G055 rev. 1445, NGC 7213 rev. 269), where a broader component was detected ($\sigma \sim 0.2$–0.7 keV, $EW \sim 80$–160 eV), which might indicate a blending, either between the ionized Fe Kα and neutral Fe Kβ or with the blue peak of a relativistic component.

The most relevant features detected in the 4–9 keV energy range of the time-averaged spectra are listed in Table 1. The revolution numbers of the corresponding observations are reported in the table. A flag indicates the significance level obtained from intensity vs energy contour plots. Multiple flags refer to the corresponding features in order of increasing energy. The single and double asterisks indicate detection significance at >4σ and between ~3σ–4σ, respectively.

3.3. Spectral variability

The spectral variability was investigated by systematically mapping residuals to the continuum emission in the time vs energy domain over the 4–9 keV band. As most of the features observed in the time-averaged spectra are unresolved in their fine structure, the chosen energy resolution for the time-energy "mapping" was 0.1 keV for nearly all the sources[2] (i.e. approximately equal to the detector resolution in the analysed band). Though not producing a good oversampling for most of the features, this energy resolution represents the only viable choice for the available data. The time resolution of the map has to be chosen in order to garantee a sufficient number of counts in each energy bin. By fixing the energy resolution, we thus extracted spectra at different time resolutions during the period of minimum flux of the source, and required a minimum of 20 counts per bin (for the χ^2 statistics to be applicable) in the Fe K complex energy band

---

[1] Pile-up was revealed in the following observations: IC 4329a rev. 210 (carried out in "FullWindow" mode), MCG-5-23-16 rev. 363 (carried out in "FullWindow" mode) and 1099 (carried out in "LargeWindow" mode), NGC 3227 rev. 1279 (carried out in "LargeWindow" mode), and ESO 141-G055 rev. 1435, 1436, and 1445 (carried out in "FullWindow" mode).

[2] In the case of NGC 4051 (rev. 541), AKN 564 (rev. 930), and MRK 704 (rev. 1074), we opted for a lower energy resolution (i.e. 0.2 keV, see Table 2) to keep a high enough time resolution.

(i.e. at least for $E < 7.5$ keV). The adopted time resolutions are listed in Table 2.

It is useful to compare the time resolutions used in the analysis with a typical time scale of the system. As an indicative time scale we can consider the estimated orbital period at 10 r_g, given by (e.g. Bardeen et al. 1972):

$$T_{orb} = 310 \left[a + (r/r_g)^{3/2} \right] M_7 \ \ (s),$$

with r_g the gravitational radius, M_7 the mass of the black hole in units of $10^7 \ M_\odot$, and a the adimensional angular momentum per unit mass. Following the Nyquist-Shannon sampling theorem, the condition $\Delta t = T_{orb}/2\beta$ (with $\beta \geq 1$ the sampling factor and Δt the chosen time resolution) must be satisfied for the chosen time resolution to oversample this characteristic time scale.

It is thus generally the case here that the estimated orbital time scale at 10 r_g is oversampled by the chosen time resolution. In only four cases, where the orbital period is very short (i.e. ≤ 2.5 ks) the time resolution cannot adequately oversample it, so that the minimum number of counts per energy is preserved. The sources for which we were forced to undersample the orbital time scale at 10 r_g are MCG-6-30-15, MRK 766, NGC 4051, and AKN 564.

The method used to produce excess time-energy maps is extensively described in IMF04 and Tombesi et al. (2007) and briefly summarized in the following:

i)   each observation was divided into slices according to the chosen time resolution;
ii) for each slice, the continuum was determined by excluding the Fe K energy band (i.e. typically at $E \sim 5$–7 keV) and by rebinning the spectrum to have at least 50 counts per energy bin to garantee a reliable continuum determination in the high-energy part of the spectrum ($E > 7.5$ keV);
iii) the baseline spectral model for the continuum is a power-law plus cold absorption (with the column density N_H parameter fixed at the value obtained from the average spectrum);
iv) data were then rebinned at the energy resolution of the map. Residuals to the best-fit continuum model were computed in the 4–9 keV energy band and visualized on a time vs energy plane;
v)   a circular Gaussian low-pass filter with $\sigma_{lp} = 0.85$ pixel is used to smooth the image in the time-energy plane so as to reduce random noise between adjacent pixels.

In the maps, signal–to–noise ratios (S/N) of residual flux are displayed (see Figs. 4–9). The noise includes contributions from uncertainties in the subtracted background and power-law model components, and in the excess residual counts.

The excess map technique is useful for identifying spectrally and temporally transient, narrow features and tracing their energy/intensity temporal evolution. As these features could appear at an energy that is not known a priori, we defined three physically motivated energy bands for the extraction of residuals light curves, which allowed inference of the statistical significance of such structures in a uniform and systematic way:

A: 5.4–6.1 keV, redshifted Fe Kα line band;
B: 6.1–6.8 keV, neutral and/or mildly ionized Fe Kα line band;
C: 6.8–7.2 keV, Fe Kβ and/or highly ionized Fe Kα band.

Even though the widths of the chosen energy bands are greater than the spectral binning of the maps, only relatively narrow features are picked up in the residuals analysis. Any other broad feature spreading across the entire width of each band would be accounted for by the continuum modelling for each time-resolved

spectrum. Moreover, adopting wider energy intervals allows an increase in the statistics of the integrated residual counts.

Light curves of the resulting excess flux and relative excess maps are reported for the observations where significant variability has been detected (see Figs. 4–9). The light curves are renormalized for their corresponding average value. In the figures the maps are all shown at a time resolution of 2.5 ks, to display excess residuals better. The procedure used to calculate the light curves errors is outlined in Sect. 3.4.

3.4. Light curve error estimation and variability significance

The excess map technique is useful for revealing narrow transient features (IMF04) and is not affected by the presence of broad line components (as the adopted continuum model would mimic the shape of these lines). The smoothing process applied (see previous section) prevents, however, direct determination of the lines significance. For instance, the errors on the flux measurements in the time series cannot be estimated using a counting statistics because, after the smoothing, adjacent pixels in the map are no longer independent, so we followed the procedure described in IMF04 to assess the errors via simulations. We simulated $N_{sim} = 1000$ time-energy maps, assuming constant spectral components (whose parameters are those of the average spectrum best-fit model, as reported in Table 3) and a power-law normalization varying as the 0.3–10 keV light curve[3]. These simulations are carried out using the *fakeit* Xspec task, which allows creation of fake source and background spectra with a Poisson noise distribution, which approaches the normal distribution whenever the number of counts per bin is >20.

The square root of the simulated light curves mean variance (in the band of interest) is thus taken as the error of the real light curve. This is justified by the Gaussian components flux being assumed constant in the simulations (and consequently equal to zero in case of no line detection), hence a measure of the variance is a good estimate of the real time series errors.

The variability significance was calculated by comparing the real light curve variance (σ_r^2) with the simulated ones (σ_s^2). If N is the number of simulated light curves for which $\sigma_s^2 > \sigma_r^2$, the variability significance is given by $(1 - N/N_{sim})$. Table 4 contains a list of the computed variability significances in the considered energy bands.

3.5. Robustness against continuum modelling and background filtering

The technique summarized above assumes a simple modelization for the underlying continuum (i.e. a power-law plus cold absorption). As this assumption may affect the flux estimation of the variable features, we tested its robustness by considering a more complex continuum model, comprising an ionized absorber component (*absori* model in Xspec, Done et al. 1992) rather than the cold absorption one. The test was performed for IC 4329a, the brightest source in the sample, with the highest statistics providing the most accurate estimate of the continuum. For each energy band, we found that the calculated residuals are within the flux errors derived by the simple power-law

---

[3] In the case of MCG-6-30-15, the curvature induced by the broad Fe line is treated as the result of continuum emission (see Appendix). Since the broad line ($E \sim 3$–7 keV) is less variable than the broad band 0.3–10 keV continuum (e.g. Vaughan & Fabian 2004), the power-law normalization is assumed to follow the 4–9 keV light curve in the simulated maps.

plus cold absorption continuum fit. On average, the difference between residuals calculated with the two continuum models is around 30% of the light curve error. This comes from several factors: the narrow band considered for the analysis (E = 4–9 keV), the high-energy resolution of the maps (suitable for studying narrow spectral features) and the lower variability level of secondary components (i.e. reflection continuum and ionized absorber systems) than the primary power-law. We conclude that the underlying continuum in the chosen bandpass is represented well by a simple power-law, with cold absorption a good enough approximation for modelling the residual curvature.

It is worth noting that the reflection continuum associated to the narrow and constant Fe Kα line dominates the one associated with any transient feature. This dominant reflection component will provide a constant contribution in the flux measurements, so it will not introduce any spurious variability in the residuals maps.

As a consequence of the adopted technique and high-energy resolution (i.e. ΔE = 0.1–0.2 keV), the maps will only be sensitive to narrow spectral features (i.e. both spectral lines and narrow structures of the relativistic line profile). We furthermore checked that the assumption of a fixed value for the cold absorption N_H parameter in the continuum subtraction process (see Sect. 3.3) can produce spurious variable features (most of all in the redshifted energy band). This might be the case, for instance, in the presence of any residual curvature induced by variable and/or complex absorbers (i.e. warm absorber) and/or more complex continuum modelling. The test is exploited for the long-look (rev. 301, 302, and 303) of MCG -6-30-15, because this source is characterized by a strongly variable X-ray flux and a complex spectrum (including both a warm absorber and a relativistic Fe line). In Fig. 1 we show a comparison between the residual line flux measurements (as obtained from the excess map analysis in band A, B, and C) for the subtracted continuum model including (1) a variable or (2) a fixed N_H. As expected, the line fluxes are well-correlated (the linear Pearson correlation coefficients are 0.68, 0.85, and 0.91 for the three bands), although the scattering from the best-fit linear model increases for lower energy bands, where the effects of continuum modelling are stronger; however, the relative error due to the deviation in the line flux (1)-flux (2) plot from the linear model is smaller than the statistical error in the line flux measurement as obtained from simulations (see Sect. 3.4). It is worth noticing that the scatter also depends on the energy and time resolutions adopted, decreasing for lower resolutions.

We conclude that our assumption of constant N_H does not invalidate our results. Since the case of MCG -6-30-15, one of those most representative of a strongly variable bright source with broad relativistic Fe line emission, we infer that this assumption can be considered valid for all the other sources in the sample. As some AGNs show a spectral steepening when they get brighter, we also tested whether significant variations in the power-law Γ parameter, which might influence the line flux measurements, are registered during each observation where significant variability in at least one of the three energy bands has been observed. The fractional deviation of the power-law index from a constant model is always $\leq$20%. We rule out the possibility that such small deviations can produce spurious variations in the line fluxes, since the statistical errors on the fluxes are generally larger. This result again validates our assumption of a constant Γ parameter in the simulations (see Sect. 3.4). Finally we exploited an a-posteriori check on the filtered background to exclude this can lead to fake results. Indeed, energy-dependence of soft-p$^+$ flares might in principle produce spurious variable
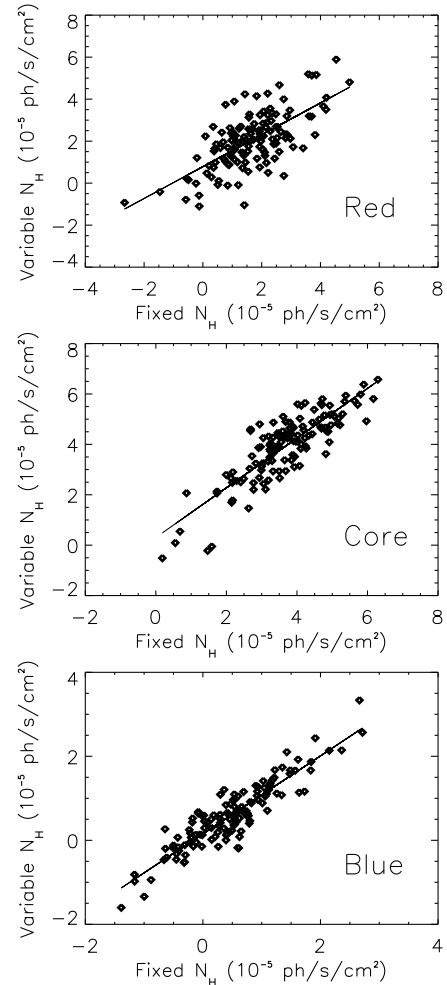

Fig. 1. Comparison between line flux measurements for subtracted continuum model including a power-law plus either a fixed or variable cold absorption N_H parameter. The fluxes are obtained from residuals in the A, B, and C energy bands (*from the top to the bottom panels*, respectively).

features in the spectrum of the source. To check this we inspected the background 4–9 keV light curves during observations where significant variability in the Fe K band was found. After soft-p$^+$ flares removal, the background contributes less than 8% to the 4–9 keV count rate in most observations. Such a low background fraction is not expected to have any effect on our results; however, during 7 of these observations, the fraction of background count rate, even after soft-p$^+$ flares removal, remains high, falling between 11% and 38% of the source one. To check that this may induce spurious energy dependent variability in the source spectrum, we inspected the background spectra during periods of maximum count rate and compared them to the time-averaged one. We fitted these spectra using a broken power-law model, obtaining in all cases a good fit. We found that the background spectral shape does not change, apart from a significant increase in normalization. This means that no energy dependence is present in flares.

4. Results from excess maps

The excess map technique revealed variability at $\geq$90% confidence level (against random noise) *within at least one* of the

three (red, rest-frame, and blue) energy bands in 26 out of 72 observations (see Table 4), whereas, the overall number of energy bands showing excess variability in the sample is 34 with significances in the range of 90–99.7% each.

To assess the statistical significance of this result, we carried out a binomial test. As we looked for variability within three distinguished energy bands (see Sect. 3.3), the total number of trials that must be taken into account in the computation is 216 (i.e. number of observations times number of analysed energy bands). Furthermore, we made the conservative assumption that all the observed variable features are detected at the lower-limit confidence threshold, i.e. 90%. The test yielded 99.5%, i.e. about 3σ, as the probability for rejection of the null hypothesis. In other words, the number of variable features detections in the sample is significantly greater than the one expected from a random distribution.

In the former calculation we conservatively assumed that the three energy bands are independent. This is justified by the fact that, during the same observation, significant variability is rarely observed in more than one band (i.e. only in 7 out of 34 cases). Although from a physical point of view we would expect the three bands to be somewhat linked in their variability properties, we must indeed take several observational effects into account that allow the three bands to be considered independently. For example, blended constant components (this effect should be dominant in band B, due to the "core" of the Fe $K\alpha$ line, which plausibly arises in the outer regions of the disk or even farther), and the fact that S/N decreases at higher energies may result in an underestimate of the variability significance in both B and C bands. As next step we tried to estimate and quantify potential observational biases and/or limits that may hamper the detection of Fe K variability.

One of the main observational issues in our analysis is the duration of the exposure. Physical considerations about the choice of the maps temporal sampling were done by referring to the orbital time scale at 10 r_g (See Sect. 3.3). This is an arbitrary choice that does not address the possibility for variability phenomena to occur on shorter time scales. However, it represents an observational bias that cannot be removed easily, because the quality of current data does not allow sampling of shorter orbital periods. In fact, in our analysis, sampling time scales must be chosen to preserve good statistics in each time-resolved spectrum, and should be able, at the same time, to probe the short-term variability of the features in the Fe K band, even of relativistic ones. Because relativistic effects are expected to still be observable at $r \sim 10$ r_g, the choice of considering the estimated orbital time scale at such a distance as a characteristic time scale of the system is justified. Unfortunately, for some of the analysed observations the total exposure is too short compared to the orbital time scale at 10 r_g. This in principle forbids detection of features varying on time scales either of this order or longer.

At the same time, the other important issue is the brightness of the source, as the possibility of obtaining significant detections depends on the total number of counts collected during the characteristic time scale of variations.

To account for these two biases, we made a further selection on the sample. We defined the figure of merit (FOM),

$$FOM = \frac{F_{2-10\ keV} \times T}{T_{orb}} \quad (\text{erg s}^{-1}\ \text{cm}^{-2}),$$

as the total 2–10 keV flux per unit area during the whole observation of duration T, normalized for the estimated orbital time scale T_{orb} at 10 r_g. This is equivalent to the total number of counts rescaled for the orbital time scale.

We arbitrarily sampled all the observations having $FOM \geq 1.4 \times 10^{-10}$ erg s^{-1} cm^{-2}, which corresponds to the inclusion of those with an exposure 10 times longer than the orbital time scale at 10 r_g and with a flux lower limit of $F_{2-10\ keV} \geq 1.4 \times 10^{-11}$ erg s^{-1} cm^{-2}. This selection yields a total number of 33 "good" observations[4] out of 72. By carrying out a binomial test on this subsample (which includes a total of 19 energy bands showing excess variability), we obtain a slightly higher probability, i.e. $P = 99.6\%$, that the recorded significant detections are not random. In the computation of FOM the main source of uncertainty is the BH mass, which affects the orbital time-scale estimate. However, in most cases we used masses derived from optical/UV reverberation mapping measurements (see Ferrarese & Ford 2005, for a discussion on the reliability of reverberation mapping technique and a comparison with other methods). We collected different mass estimates (see references in Table 3), obtained either via direct reverberation measurements or through secondary mass estimators based on reverberation mapping, from the recent literature (Wang & Zhang 2007; Peterson et al. 2004; Bian & Zhao 2003; Kaspi et al. 2000; and Ho 1998). For each source, we used the average mass value in the calculation of T_{orb} (see Table 3). In four cases (MCG -5-23-16, NGC 7314, MR 2251-178, and ESO 511-G030), reverberation mapping measurements were not available, so mass estimates from other methods were adopted (e.g. the photoionization method, Wandel & Mushotsky 1986; Padovani & Rafanelli 1988, or accretion disk-model spectral fitting, Brunner et al. 2007). In those sources (MCG -6-30-15, NGC 526A, ESO 198-G024, AKN 564, and NGC 7213) where only one reverberation mass value was found in literature, available estimates from different methods were added in the computation of the average mass. Figure 2 shows the distribution of variability significances in the three bands from this subsample.

Assuming that statistical fluctuations dominate the observed variability in the data, we would expect the distribution of significances to be flat. Indeed, in this case, variances in the real data greater than those observed in the simulated light curves would be recorded 10% of the time with significances below 10%, 10% of the time with significances between 10%–20%, and so on, leading to a flat probability density distribution. The dashed histogram in Fig. 2 illustrates the distribution of significances derived from simulated data whose variability stems from random fluctuations (assuming the same total number of observations as the real ones). We observe that the var-sig distribution is significantly peaked at high values, with a deficit at low significances, thus indicating the effective presence of the features we are finding. In particular, a K-S test strongly contradicts the observed distribution as consistent with the random one ($P_{KS} = 0.13\%$). Moreover, if we only focus on band A and C where relativistic, energy shifted (either redwards or bluewards) features are expected to be detectable (Fig. 3), the clustering towards high significance results even more prominent ($P_{KS_{red+blue}} = 0.06\%$). Conversely, the distribution is smoother and similar to the random one (Fig. 3) when the energy band containing the narrow "core" of the $E = 6.4$ keV Fe $K\alpha$ component is isolated ($P_{KS_{core}} = 62\%$). This effect is indeed expected, since the narrow component contributes with an almost steady flux to the total

---

[4] IC 4329a (rev. 670), MCG -5-23-16 (rev. 1099), NGC 3783 (rev. 193, 371, 372), NGC 3516 (rev. 245, 1250, 1251, 1252, 1253), MCG-6-30-15 (rev. 108A, 108B, 301, 302, 303), NGC 7314 (rev. 256, 1172), NGC 3227 (rev. 1279), MRK 766 (rev. 82, 265, 999, 1000, 1001, 1002, 1003, 1004), NGC 7469 (rev. 912, 913), NGC 4051 (rev. 263, 541), MRK 110 (rev. 904), AKN 564 (rev. 930), NGC 4593 (rev. 465).
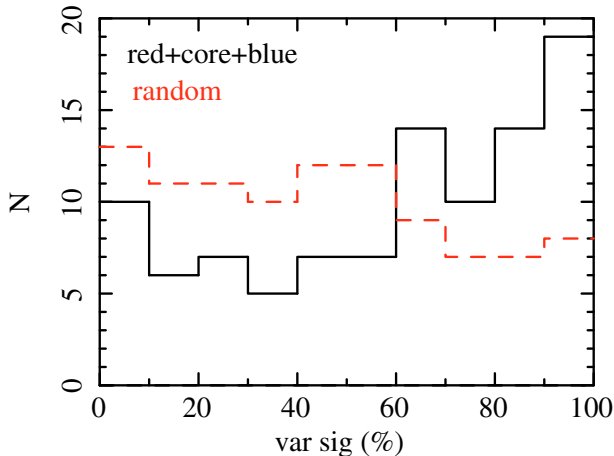
Fig. 2. Distribution of variability significances in the three analysed energy bands of the *FOM*-selected sub-sample (continuous curve). The dashed curve represents the distribution obtained from simulations whose variability is produced by random fluctuations.
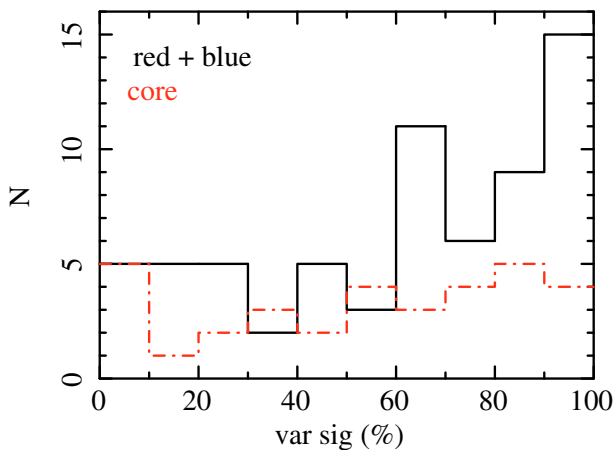

Fig. 3. Distribution of variability significances of the *FOM*-selected subsample: comparison between the "core" (B band, dashed line) and the "red+blue" (bands A and C, continuous line) distributions.

band counts being most plausibly produced in regions far from the nucleus.

5. Summary and discussion

The main goal of this paper is to find and monitor transient emission and absorption features in the Fe K line energy band of radio-quiet and bright AGNs. Because the detection of transient features is seriously biased by the lack of good statistics (time-resolved spectra are usually characterized by low S/N, which in most cases prevents obtaining high significance detections), the best method to derive strong conclusions on their reliability is by analysing a statistically complete sample. This issue is addressed in the present work for the first time, where we present both null and positive results from the uniform analysis of an almost (94%) complete sample of sources, allowing statistically meaningful conclusions to be drawn.

In this respect we studied a flux-selected subsample of the FERO sample, defined by GBD06. The sample includes the 30 brightest (in the RXTE Slew Survey, XSS, with a flux lower limit of $F_{2-10 \, keV} \geq 1.5 \times 10^{-11}$ erg cm^{-2} s^{-1}) radio-quiet AGNs observed by XMM-*Newton* as of 1 February 2009. The observations we analysed (for a total of 72) were chosen to have a

duration $\geq$10 ks, in order to carry out a meaningful temporal analysis.

Adopting the method of searching for excess variability (IMF04) in the energy bands of the redshifted (band A), neutral-mildly ionized (band B), and highly ionized Fe Kα and/or neutral Fe Kβ (band C) lines, we revealed significant (with a confidence level $\geq$90%) signatures of variable features in 26 out of 72 observations, with probabilities in the 90%–99.7% range. Considering the total number of energy bands showing excess variability, this translates into 34 detections out 216 monitored energy bands. A binomial test for the significance of this result yielded a probability of 99.5% (i.e. ~3σ) that the overall detections are not by chance.

We then tested the detection frequency of variable features, after taking several observational biases into account (i.e. short duration of the exposure as compared with a typical dynamical time scale of the system, as well as low flux observations) which might seriously prevent positive detections. We tried to remove these biases by defining an *FOM* ratio (see Sect. 4). As these observational limits forbid us drawing conclusions about Fe K variability properties in the faintest sources of the sample, we focus the following discussion on the *FOM*-selected dataset. Once the selection is accomplished, the distribution of variability significances in the three energy bands (with significant detections ranging from 91.7% to 99%), results peaked towards high values (i.e. $\geq$90%). Moreover, subtracting the contribution of the "core" energy band (band B), which is not expected to show signatures of strong variability due to the dominance of the constant Fe Kα emission, the skewness of the distribution towards high significance increases. All these results were statistically checked through a K-S test, using a uniform distribution as the reference one.

From the significances distribution analysis, it is reliable to assert that variability is commonly observed in the Fe K complex energy band of bright sources (see Fig. 2), provided the typical variability time scale is sampled well by the duration of the observation and the source is sufficiently bright. In fact, our estimated detection frequency is of 13 observations out of 33, showing variability in at least one of the three sampled energy bands, i.e. ~39%. Moreover, from Fig. 3 it is clear that the bulk of variability comes from the red- and blue-shifted (with respect to the neutral "core") energy bands. This is most probably because, if variability phenomena are still taking place in the neutral Fe Kα band, they end up being overwhelmed by the constancy (on short time scales) of the Fe line "core". Indeed, the detection frequency of variable features in the red- plus blue-shifted energy bands is 12 out of 33 observations, i.e. ~36%. It is worth noting that this is very similar to the fraction of observations (i.e. 12/37 ~ 32%) for which the characteristic emission radius of the relativistic component is constrained to be <50 r_g in the NOGR07 sample.

Understanding the origin of the variable features in our sample from current data is not easy. Any excess of variability recorded in band A most probably stems from redshifted Fe K emission. Indeed this energy band, apart from the relativistic Fe K line components, is expected to include only the Fe Kα high-order Compton shoulders, which, however, are predicted to be very faint (e.g. George & Fabian 1991; Matt 2002). It has been claimed that partial covering can induce spectral curvature in this band (e.g. Miller et al. 2008). Indeed, an ionized complex absorbing system might introduce further complexity and be responsible for variability as a consequence of variations in its properties (e.g. ionization state, covering factor, etc.). Although hard to predict, we expect that, in general, the partial covering

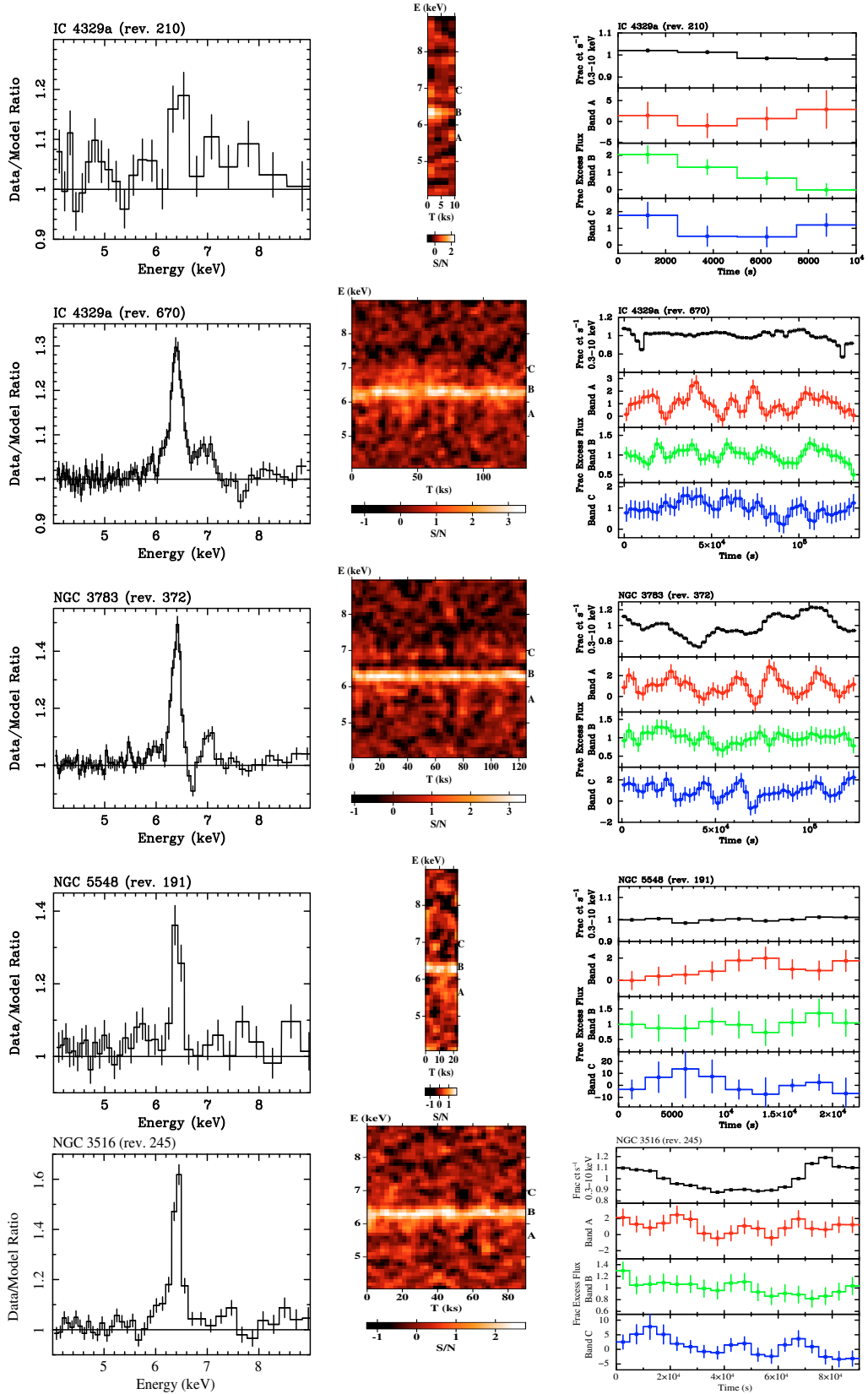**Fig. 4.** *Left panels*: data-to-model (power-law plus cold absorption) ratios of the 4–9 keV time-averaged spectra; *middle panels*: S/N map of excess residuals in the time-energy plane (at a time resolution of 2500 s); *right panels*: 0.3–10 keV background subtracted continuum and residuals light curves (in bands A, B, and C). The light curves are renormalized for the corresponding average flux.

Table 4. Variability significances obtained from excess map analysis in the three energy bands: 5.4–6.1 keV (band A), 6.1–6.8 keV (band B), and 6.8–7.2 keV (band C). Confidence levels ≥90% are marked in boldface.

Sources	band A (%)	band B (%)	band C (%)	Sources	band A (%)	band B (%)	band C (%)
IC 4329a (rev. 210)	35.8	**99.7**	71.2	MRK 590 (rev. 837)	71.3	11.6	6.8
IC 4329a (rev. 670)	**98.5**	74.5	11.2				
				MRK 766 (rev. 82)	20.3	32.2	45.0
MCG -5-23-16 (rev. 363)	31.0	77.3	66.9	MRK 766 (rev. 265)	1.4	80.2	49.5
MCG -5-23-16 (rev. 1099)	63.2	79.8	89.5	MRK 766 (rev. 999)	70.8	38.8	71.0
				MRK 766 (rev. 1000)	45.6	60.7	3.1
NGC 3783 (rev. 193)	36.7	25.6	82.7	MRK 766 (rev. 1001)	47.6	59.8	70.8
NGC 3783 (rev. 371)	68.1	5.3	58.3	MRK 766 (rev. 1002)	84.7	70.0	66.1
NGC 3783 (rev. 372)	**96.7**	5.3	65.2	MRK 766 (rev. 1003)	**97.2**	84.6	29.9
				MRK 766 (rev. 1004)	**95.7**	**95.6**	24.3
NGC 5548 (rev. 191)	61.9	6.8	**94.3**				
NGC 5548 (rev. 290)	23.0	82.9	74.7	NGC 7469 (rev. 192A)	42.9	4.6	**96.6**
NGC 5548 (rev. 291)	77.3	51.1	14.9	NGC 7469 (rev. 192B)	81.6	40.5	**94.5**
				NGC 7469 (rev. 912)	84.5	86.9	86.7
NGC 3516 (rev. 245)	30.2	28.6	**98.2**	NGC 7469 (rev. 913)	66.6	43.3	3.4
NGC 3516 (rev. 352)	88.6	29.6	6.5				
NGC 3516 (rev. 1250)	14.4	88.7	**95.7**	MCG -2-58-22 (rev. 180)	54.4	44.9	49.4
NGC 3516 (rev. 1251)	**91.7**	62.8	**93.7**				
NGC 3516 (rev. 1252)	67.9	39.8	**99**	NGC 526A (rev. 647)	78.7	58.7	52.3
NGC 3516 (rev. 1253)	77.0	4.2	66.6				
				NGC 4051 (rev. 263)	65.4	57.9	78.3
MRK 509 (rev. 161)	**95.3**	**90.4**	42.3	NGC 4051 (rev. 541)	20.3	53.4	82.3
MRK 509 (rev. 250)	66.1	3.1	72.2				
MRK 509 (rev. 1073)	**92.7**	13.7	88.1	ESO 141-G055 (rev. 1435 A)	**93.4**	9.0	**93.0**
MRK 509 (rev. 1074)	83.7	30.0	25.1	ESO 141-G055 (rev. 1435 B)	13.0	12.8	20.8
MRK 509 (rev. 1168)	27.1	**91.2**	65.8	ESO 141-G055 (rev. 1436)	19.1	20.8	15.8
				ESO 141-G055 (rev. 1445)	60.7	59.8	10.7
MCG -6-30-15 (rev. 301)	**97.0**	82.5	**93.7**				
MCG -6-30-15 (rev. 302)	63.7	**96.5**	82.8	UGC 3973 (rev. 1247)	70.6	37.8	52.3
MCG -6-30-15 (rev. 303)	83.1	67.4	4.7	UGC 3973 (rev. 1263)	**94.6**	41.5	74.7
MCG -6-30-15 (rev. 108A)	81.6	79.6	65.4	UGC 3973 (rev. 1332)	37.3	48.4	16.2
MCG -6-30-15 (rev. 108B)	**97.0**	**96.4**	**94.5**	UGC 3973 (rev. 1535)	55.6	24.7	**95.9**
MCG +8-11-11 (rev. 794)	14.1	29.9	20.3	Fairall 9 (rev. 105)	71.8	25.6	82.9
				ESO 198-G024 (rev. 207)	**92.4**	54.7	35.4
NGC 7314 (rev. 256)	**96.2**	43.3	67.2	ESO 198-G024 (rev. 1128)	86.7	27.6	2.7
NGC 7314 (rev. 1172)	70.9	11.5	17.1				
				MRK 110 (rev. 904)	27.7	5.6	56.8
AKN 120 (rev. 679)	62.5	44.0	45.9				
				AKN 564 (rev. 930)	12.1	**94.0**	**95.5**
MRK 279 (rev. 1087)	64.1	44.0	66.0				
MRK 279 (rev. 1088)	17.5	69.1	31.1	NGC 7213 (rev. 269)	64.7	79.2	67.1
MRK 279 (rev. 1089)	14.1	3.6	**94.5**				
				ESO 511-G030 (rev. 1042)	44.3	87.5	11.8
MR 2251-178 (rev. 447)	58.2	72.3	83.4				
				MRK 704 (rev. 1074)	85.7	**91.3**	15.5
NGC 3227 (rev. 178)	72.4	26.4	32.2	MRK 704 (rev. 1630)	36.8	58.2	78.0
NGC 3227 (rev. 1279)	40.9	53.4	17.4				
				NGC 4593 (rev. 465)	9.2	9.9	54.0
IRAS 05078+1626 (rev. 1410)	24.3	21.7	9.8				

gas would imprint its signature in the *B* band, as well as in the A and C bands. The plot of Fig. 3 conversely, clearly shows a lack of correlated variations between the "core" and the "red+blue" energy bands, disproving the partial covering interpretation.

On the other hand, the other two bands, in addition to the constant (on short time scales) Fe Kα and Fe Kβ emission components, can also include both the blue peak of a relativistic Fe line and ionized Fe K absorption features, which may also be responsible for the detected variability. Differentiating the two cases would require deeper analysis of any single case. However, residuals observed in band B are always positive, which is correct for the variable features in emission. In contrast, there are three cases (NGC 3516 rev. 1250, 1251, and 1252) where variable residuals in band C are negative, hence most probably due

to variable absorption features. This view is confirmed by the detection of two absorption lines in the time-averaged spectra of the three observations at these energies. In all the other cases, the average residuals flux in band C is positive, pointing to an origin in emitting material, most probably the peak of a relativistic Fe line. Assuming this is the viable interpretation, we can give 10/33, i.e. ~30%, as an estimate for the detection frequency of relativistic variable features in bright and radio-quiet type 1 AGN, again close to the fraction deduced by NOGR07.

Inspection of residual light curves of the entire sample allows us to roughly compute the time scale on which the observed variations take place. In almost all the cases, these variations do not have a regular shape. Only in three cases (IC 4329a rev. 670, NGC 3783 rev. 372, and MRK 509 rev. 1073) are they characterized by a repeated, flare-like pattern. For these and other observations, a deeper study can be undertaken (i.e. NGC 3516, IMF04; MKN 766, Turner et al. 2006; NGC 3783, Tombesi et al. 2007; IC 4329a, De Marco et al. 2009), and we refer to the related papers for an exhaustive discussion. In general, we decided to assume the time interval between the maximum peak in the light curve along with either the following or the preceding flux minimum as the temporal time scale of the variations. The range of estimated time scales is $\Delta t = 6$–30 ks. This allows computation of an upper limit to the extension of the region responsible for the observed variations. As variability from a source cannot be observed on time scales shorter than the light crossing time of the source itself, the upper limit on the size of the region is given by $R < c\Delta t$ (e.g. Mushotzky et al. 1993). If we consider the average $\langle \Delta t \rangle \sim 15.5$ ks (also the average value of the FOM-selected subsample) as the reference, the derived upper limit on the region extension is $R \leq 4.6 \times 10^{14}$ cm ~ 140 $r_{\rm g}$ for a black hole mass equal to the average value of the masses in the entire sample, i.e. $\langle M_{\rm BH} \rangle \sim 2.2 \times 10^7$ $M_\odot$. These calculations point to an origin in relatively small regions.

Whether these regions are flare-illuminated zones of the accretion disk or blobs of outflowing gas is not clear from our data, as the sensitivity of the observations overall does not allow tracing a clear pattern of variability. If associated to orbital motions, the observed variability would imply an average emitting radius of $\langle r \rangle \sim 7.9$ $r_{\rm g}$ (assuming the average values of $\langle \Delta t \rangle \sim 15.5$ ks and $\langle M_{\rm BH} \rangle \sim 2.2 \times 10^7$ $M_\odot$ for the time scale and the black hole mass, respectively). However, in most of the cases detection of significant variability does not come with clear intensity modulations in the observed light curves, disfavouring the "hot spot" interpretation (e.g. Nayakshin & Kazanas 2001; Dovčiak et al. 2004; Goosmann et al. 2007). Nevertheless, this does not completely rule the model out, because the estimate of spot-induced modulations significance strongly depends on the possibility of observing the spot emission for long enough (e.g. Vaughan 2005). This ultimately relies on the length of the observation and the permanence of the primary source flare. Moreover, several flare events illuminating the disk are expected to generate more complex line patterns.

While a discrete spot-like region of the disk would produce a smooth intensity/energy modulation pattern as a consequence of its orbital motion, this would not be the case if the emitting region has a ring-like geometry. In that instance, the energy modulations are expected to be weak, in agreement with results from extensive analysis of the variability patterns in some observations of our sample (NGC 3783, Tombesi et al. 2007; IC 4329a, De Marco et al. 2009). Many authors point out the possibility of producing spiral density waves in non-self-gravitating models of accretion disks (e.g. Caunt & Tagger 2001; Hawley 2001). The effects of such structures on the Fe emission line would

essentially be the production of several smaller peaks into the line profile, characterized by quasi-periodic variability as a consequence of the motion, and independent of continuum variations (e.g. Karas et al. 2001; Hartnoll & Blackman 2002).

Another suggested scenario is the production of line emission (via recombination of highly ionized Fe), during the ejection phase of blobs of gas originating from disk instabilities (Wang et al. 2000). In this case, detection of both red- and blueshifted lines from both sides of the jet are expected. Some of the observed variable features in our sample are consistent with this picture, which is not able, however, to explain the modulations registered in some sources (e.g. NGC 3516, IMF04; MKN 766, Turner et al. 2006; NGC 3783, Tombesi et al. 2007; IC 4329a, De Marco et al. 2009).

The present work is the first attempt to search for such patterns of variability. It makes use of the best quality data available up to now for this kind of study. However, distinguishing among possible interpretations is still quite difficult. A qualitative step forward in the understanding of these issues will be provided by forthcoming missions, such as the International X-ray Observatory (IXO).

References

Ballantyne, D. R., Fabian, A. C., & Iwasawa, K. 2004, MNRAS, 354, 839
Bardeen, J. M., Press, & W. H., Teukolsky, S. A. 1972, ApJ, 178, 347
Bian, W., & Zhao, Y. 2003, MNRAS, 343, 164
Bianchi, S., Matt, G., Balestra, I., Guainazzi, M., & Perola, G. C. 2004, A&A, 422, 65
Blustin, A. J., Branduardi-Raymont, G., Behar, E., et al. 2002, A&A, 392, 453
Botte, V., Ciroi, S., Rafanelli, P., & Di Mille, F. 2004, AJ, 127, 3168
Braito, V., Reeves, J. N., Dewangan, G. C., et al. 2007, ApJ, 670, 978
Brunner, H., Mueller, C., Friedrich, P., et al. 1997, A&A, 326, 885
Cappi, M. 2006, AN, 327, 1012
Cappi, M., Tombesi, F., Bianchi, S., et al. 2009 [arXiv:0906.2438]
Caunt, S. E., & Tagger, M. 2001, A&A, 367, 1095
Dabrowski, Y., & Lasenby, A. N. 2001, MNRAS, 321, 605
Dadina, M., Cappi, M., Malaguti, G., Ponti, G., & de Rosa, A. 2005, A&A, 442, 461
De Marco, B., Cappi, M., Dadina, M., & Palumbo, G. G. C. 2006, AN, 327, 1028
De Marco, B., et al. 2009, in preparation
Dewangan, G. C., Griffiths, R. E., & Schurch, N. J. 2003, ApJ, 592, 52
Done, C., Mulchaey, J. S., Mushotzky, R. F., & Arnaud, K. A. 1992, ApJ, 395, 275
Dovčiak, M., Bianchi, S., Guainazzi, M., Karas, V., & Matt G. 2004, MNRAS, 350, 745
Fabian, A. C., Rees, M. J., Stella, L., & White, N. E. 1989, MNRAS, 238, 729
Fabian, A. C., Iwasawa, K., Reynolds, C. S., & Young, A. J. 2000, PASP, 112, 1145
Ferrarese, L., & Ford, H. 2005, SSRv, 116, 523
George, I. M., & Fabian, A. C. 1991, MNRAS, 249, 352
Goosmann, R. W., Mouchet, M., Czerny, B., et al. 2007, A&A, 475, 155
Guainazzi, M., Bianchi, S., & Dovčiak, M. 2006, AN, 327, 1032 (GBD06)
Hartnoll, S. A., & Blackman, E. G. 2002, MNRAS, 332, 1
Hawley, J. F. 2001, ApJ, 554, 534
Ho, L. C. 1998, in Observational Evidence for Black Holes in the Universe, ed. S. K. Chakrabarti (Dordrecht: Kluwer), 157
Iwasawa, K., & Miniutti, G. 2004, PThPS, 155, 247
Iwasawa, K., Miniutti, G., & Fabian, A. C. 2004, MNRAS, 355, 1073 (IMF04)
Karas, V., Martocchia, A., & Subr, L. 2001, PASJ, 53, 189

Kaspi, S., Smith, P. S., Netzer, H., et al. 2000, ApJ, 533, 631
Longinotti, A. L., Bianchi, S., Guainazzi, M., Roa-Llamazares, J., & Santos-
    Lleo, M. 2007, The Multicolored landscape of compact objects and their ex-
    plosive origins, AIP Conf. Proc., 924, 795
Longinotti, A. L., Bianchi, S., Ballo, L., de La Calle, I., & Guainazzi, M., 2009,
    MNRAS, 394, 1
Markowitz A., Reeves, J. N., & Braito, V. 2006, 646, 783
Markowitz, A., Reeves, J. N., George, I. M., Braito, V., et al. 2009, ApJ, 691,
    922
Martocchia, A., & Matt, G. 1996, MNRAS, 282, L53
Matt, G. 2002, MNRAS, 337, 147
Miller, L., Turner, T. J., Reeves, J. N., et al. 2006, A&A, 453, 13
Miller, L., Turner, T. J., & Reeves, J. N. 2008, A&A, 483, 437
Miniutti, G., & Fabian, A. C. 2004, MNRAS, 349, 1435
Miniutti, G., & Fabian, A. C. 2005, to appear in Kerr Spacetime: Rotating Black
    Holes in General Relativity, ed. D. L. Wiltshire, M. Visser, & S. M. Scott
    (Cambridge Univ. Press) [arXiv:astro-ph/0507409]
Mushotzky, R. F., Done, C., & Pounds, K. A. 1993, ARA&A, 31, 717
Nandra, K., O'Neill, P. M., George, I. M., & Reeves, J. N. 2007, MNRAS, 382,
    194 (NOGR07)
Nayakshin, S., & Kazanas, D. 2001, ApJ, 553, 141
Nelson, C. H., & Whittle, M. 1995, ApJS, 99, 67
Padovani, P., & Rafanelli, P. 1988, A&A, 205, 53
Papadakis, I. E., Kazanas, D., & Akylas, A. 2005, ApJ, 631, 727
Papadakis, I. E., Brinkmann, W., Page, M. J., McHardy, I., & Uttley, P. 2007,
    A&A, 461, 931
Peterson, B. M., Ferrarese, L., Gilbert, K. M., et al. 2004, ApJ, 613, 682
Petrucci, P. O., Ponti, G., Matt, G., et al. 2007, A&A, 470, 889
Ponti, G., Cappi, M., Dadina, M., & Malaguti, G. 2004, A&A, 417, 451
Ponti, G., Miniutti, G., Cappi, M., et al. 2006, MNRAS, 368, 903
Ponti, G., Cappi, M., Vignali, C., et al. 2009, MNRAS, 236
Porquet, D., Uttley, P., Reeves, J. N., et al. 2007, A&A, 473, 67
Reeves, J. N., Nandra, K., George, I. M., et al. 2004, ApJ, 602, 648
Revnivtsev, M., Gilfanov, M., & Churazov, E. 1999, A&A, 347, 23
Revnivtsev, M., Sazonov, S., Jahoda, K., & Gilfanov, M. 2004, A&A, 418, 927
Reynolds, C. S., & Nowak, M. A. 2003, Phys. Rep., 377, 389
Risaliti, G., Bianchi, S., & Matt, G., et al. 2005, ApJ, 630, 129
Rokaki, E., & Boisson, C. 1999, MNRAS, 307, 41
Tombesi, F., De Marco, B., Iwasawa, K., et al. 2007, A&A, 467, 1057
Tombesi, F., et al. 2009, in preparation
Turner, T. J., Romano, P., & George, I. M. 2001, ApJ, 561, 131
Turner, T. J., Mushotzky, R. F., Yaqoob, T., et al. 2002, ApJ, 574, 123
Turner, T. J., Kraemer, S. B., George, I. M., Reeves, J. N., & Bottorff, M. C.
    2005, ApJ, 618, 155
Turner, T. J., Miller, L., George, I. M., & Reeves, J. N. 2006, A&A, 445, 59
Turner, T. J., Reeves, J. N., Kraemer, S. B., & Miller, L. 2008, A&A, 483, 161
Vaughan, S. 2005, A&A, 431, 391
Vaughan, S., & Fabian, A. C. 2004, MNRAS, 348, 1415
Vaughan, S., & Uttley, P. 2008, MNRAS, 390, 421
Vaughan, S., Fabian, A. C., & Nandra, K. 2003, MNRAS, 339, 1237
Wandel, A., & Mushotzky, R. F. 1986, ApJ, 306, 61
Wang, J.-M., & Zhang, E.-P. 2007, ApJ, 660, 1072
Wang, J.-M., Yuan, Y.-F., Wu, M., & Kusunose, M. 2000, ApJ, 541, 41
Watson, M. G., Auguères, J.-L., Ballet, J., et al. 2001, A&A, 365, 51
Wilms, J., Reynolds, C. S., Begelman, M. C., et al. 2001, MNRAS, 328, 27
Yaqoob, T., George, I. M., Kallman, T. R., et al. 2003, ApJ, 596, 85

Fig. 5. *Left panels*: data-to-model (power-law plus cold absorption) ratios of the 4–9 keV time-averaged spectra; *middle panels*: S/N map of excess residuals in the time-energy plane (at a time resolution of 2500 s); *right panels*: 0.3–10 keV background subtracted continuum and residuals light curves (in bands A, B, and C). The light curves are renormalized for the corresponding average flux.
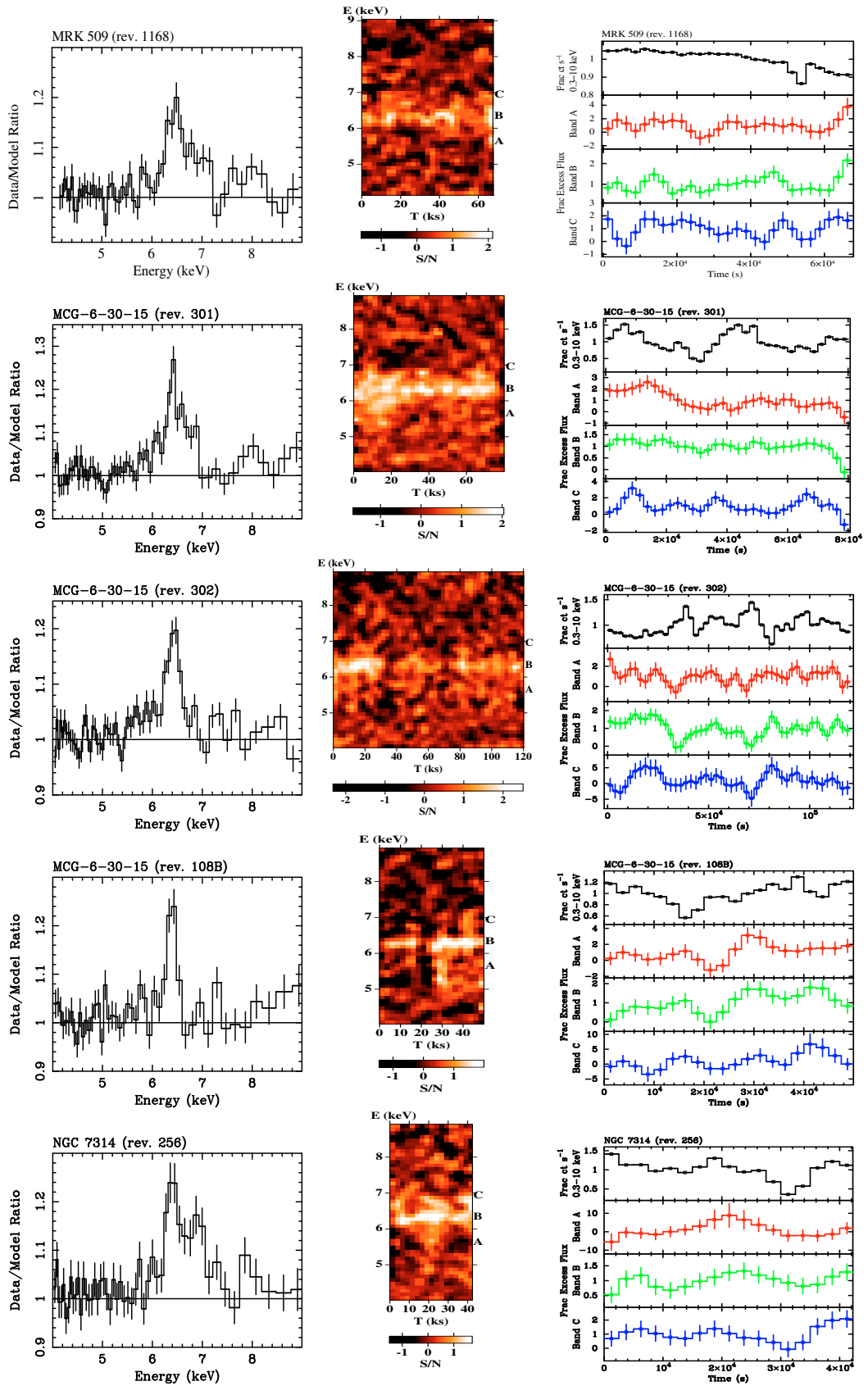
Fig. 6. *Left panels*: data-to-model (power-law plus cold absorption) ratios of the 4–9 keV time-averaged spectra; *middle panels*: S/N map of excess residuals in the time-energy plane (at a time resolution of 2500 s); *right panels*: 0.3–10 keV background subtracted continuum and residuals light curves (in bands A, B, and C). The light curves are renormalized for the corresponding average flux.
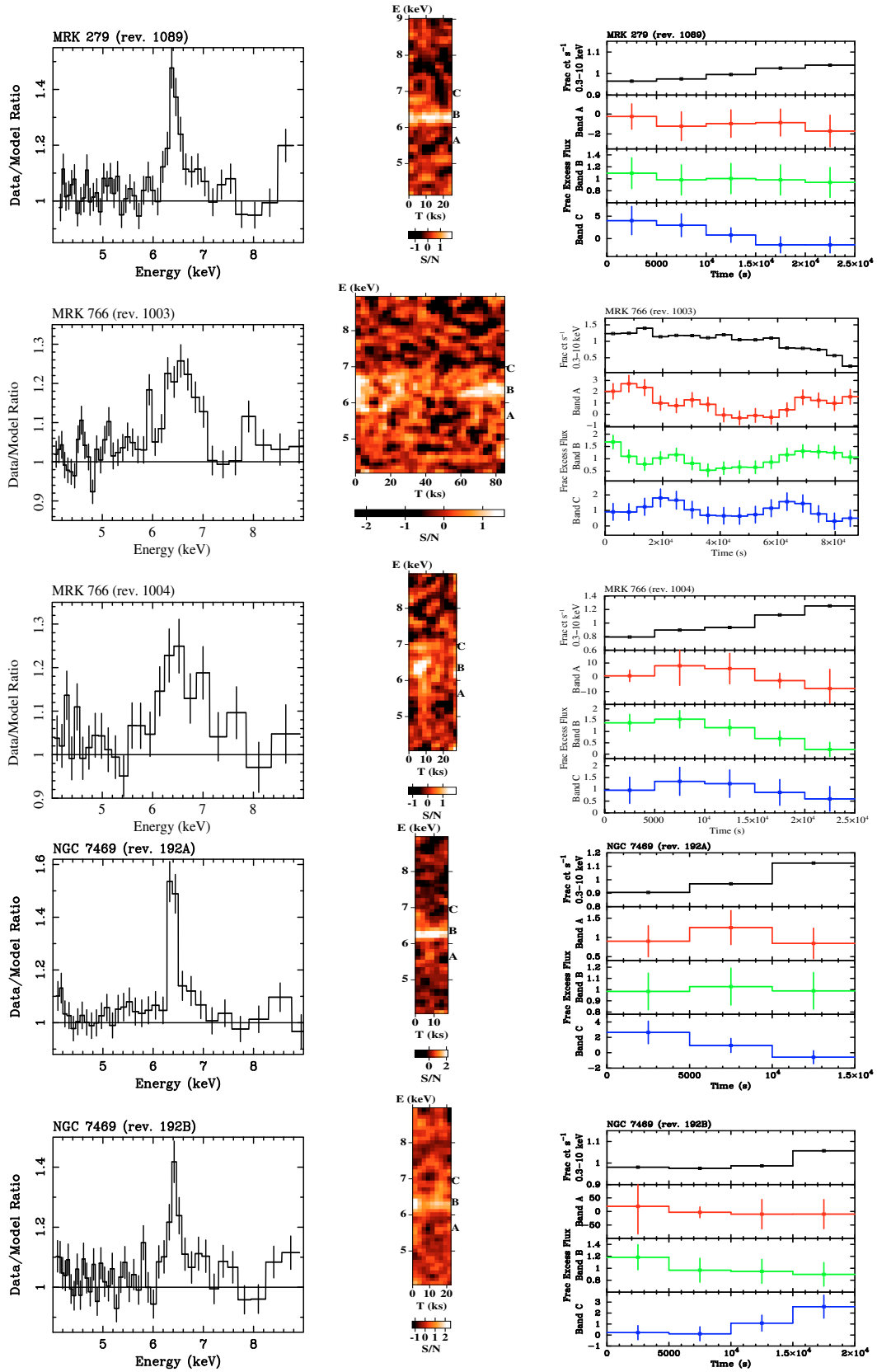
Fig. 7. *Left panels*: data-to-model (power-law plus cold absorption) ratios of the 4–9 keV time-averaged spectra; *middle panels*: S/N map of excess residuals in the time-energy plane (at a time resolution of 2500 s); *right panels*: 0.3–10 keV background subtracted continuum and residuals light curves (in bands A, B, and C). The light curves are renormalized for the corresponding average flux.
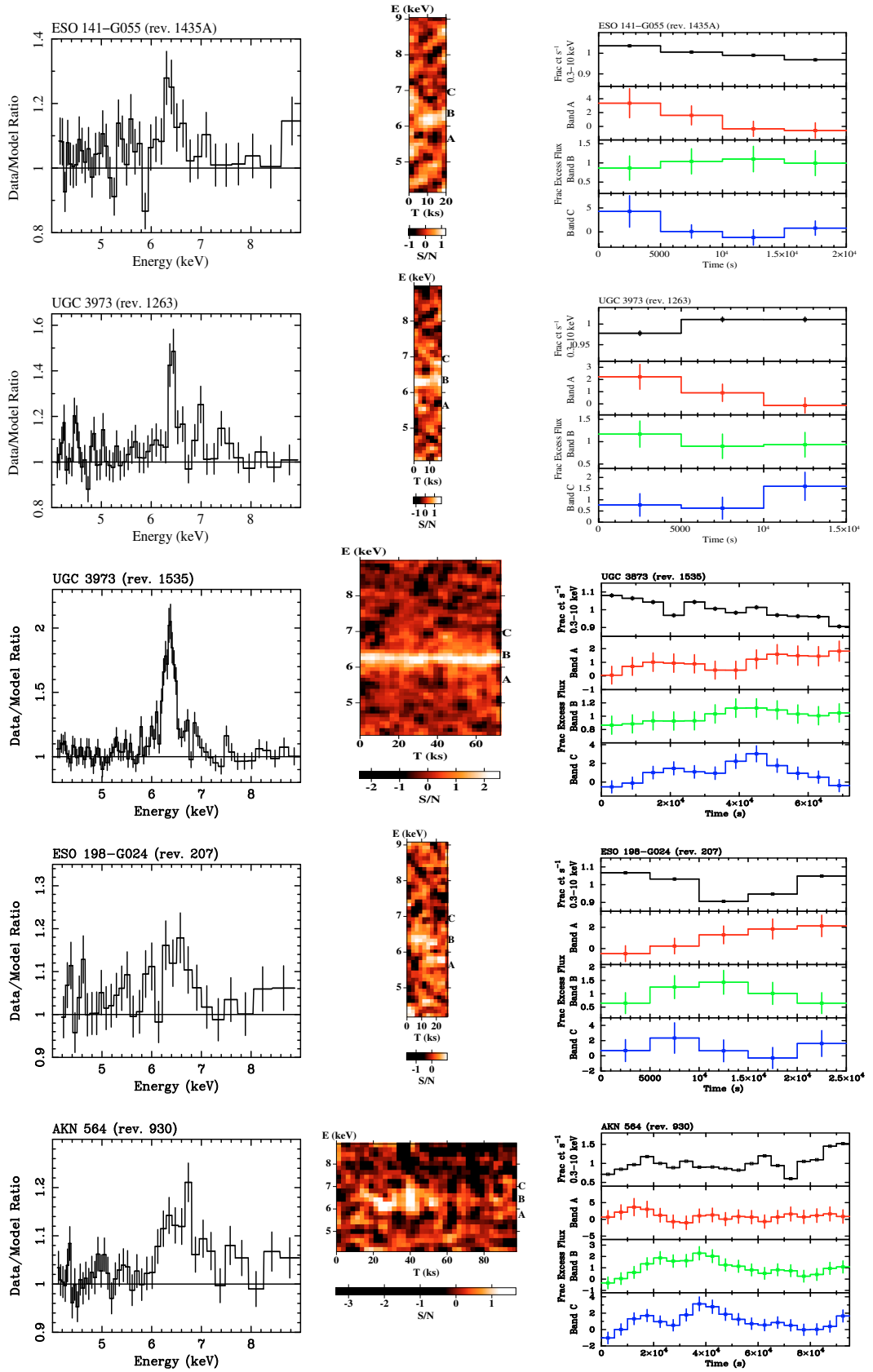
Fig. 8. *Left panels*: data-to-model (power-law plus cold absorption) ratios of the 4–9 keV time-averaged spectra; *middle panels*: S/N map of excess residuals in the time-energy plane (at a time resolution of 2500 s); *right panels*: 0.3–10 keV background subtracted continuum and residuals light curves (in bands A, B, and C). The light curves are renormalized for the corresponding average flux.

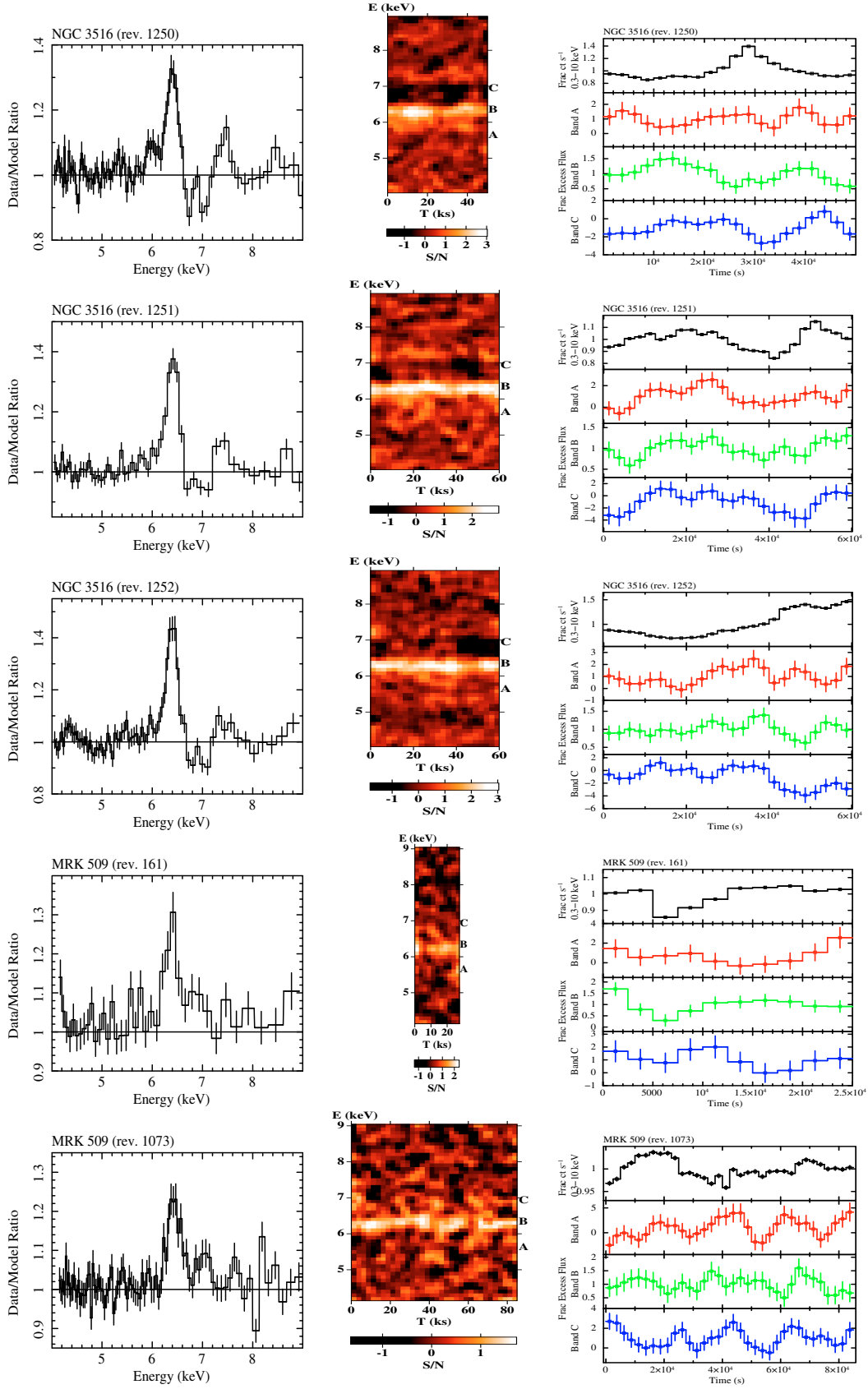**Fig. 9.** *Left panels*: data-to-model (power-law plus cold absorption) ratios of the 4–9 keV time-averaged spectra; *middle panels*: S/N map of excess residuals in the time-energy plane (at a time resolution of 2500 s); *right panels*: 0.3–10 keV background subtracted continuum and residuals light curves (in bands A, B, and C). The light curves are renormalized for the corresponding average flux.
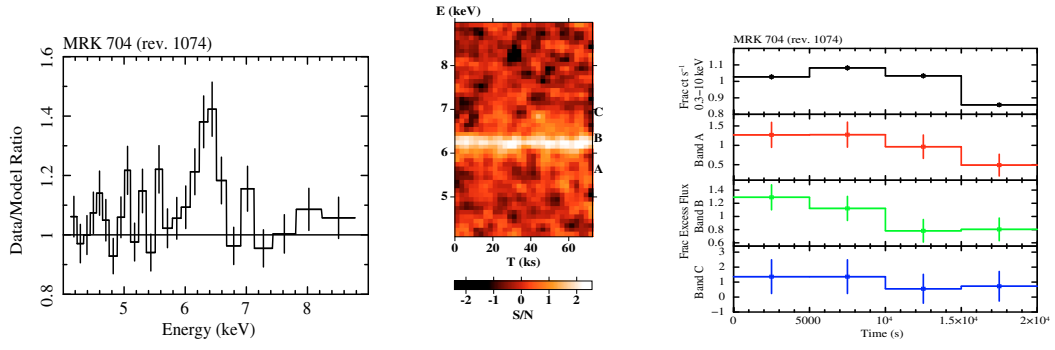
Table 2. Properties of the sources in the sample. The analysed XMM-*Newton* observations are indicated by the revolution number.

Sources	RXTE (cts/s)	z	⟨Log($M_{BH}/M_\odot$)⟩	⟨T_{orb}($10^3 r_g$)⟩ (ks)	Ref.	Rev. Num.	$F_{2-10\ keV}$ (10^{-11} erg cm^{-2} s^{-1})	Obs. Duration (ks)	Δt (ks)	ΔE (keV)	FOM (10^{-11} erg cm^{-2} s^{-1})	Γ	N_H (10^{22} cm^{-2})
(1)	(2)	(3)	(4)	(5)	(6)	(7)	(8)	(9)	(10)	(11)	(12)	(13)	(14)
IC 4329a	7.29	0.0161	7.29	19	1,2,3,4	210	15.3	10	2.5	0.1	8.0	$2.04^{+0.16}_{-0.08}$	$2.66^{+2.13}_{-2.27}$
MCG -5-23-16	6.46	0.0085	7.60	39	13	670	9.48	133	2.5	0.1	65.8	$1.73^{+0.08}_{-0.04}$	$0.35^{+0.67}_{-0.16}$
						363	7.43	22	2.5	0.1	4.2	$1.69^{+0.10}_{-0.10}$	<3.50
NGC 3783	4.90	0.0097	7.01	10	1,2,3,4,5	1099	8.29	122	2.5	0.1	25.9	$1.79^{+0.05}_{-0.05}$	$2.67^{+0.50}_{-0.50}$
						193	5.27	37	2.5	0.1	19.7	$1.86^{+0.05}_{-0.05}$	$2.80^{+0.57}_{-0.94}$
						371	5.56	131	2.5	0.1	52.3	$1.67^{+0.20}_{-0.06}$	$2.56^{+0.50}_{-0.70}$
						372	3.96	136	2.5	0.1	76.3	$1.82^{+0.03}_{-0.03}$	1.61 ± 1.10
NGC 5548	3.58	0.0170	7.71	50	1,2,3,4,5	191	3.14	23	2.5	0.1	1.4	$1.67^{+0.11}_{-0.07}$	<1.54
						290	3.86	93	2.5	0.1	7.1	$1.77^{+0.07}_{-0.06}$	<1.54
						291	4.89	37	2.5	0.1	3.6	1.89 ± 0.10	<1.83
NGC 3516	3.21	0.0088	7.21	16	1,2,3,5	245	2.34	128	2.5	0.1	19.2	1.81 ± 0.09	$5.32^{+1.16}_{-1.12}$
						352	1.53	129	5.0	0.1	12.4	$1.82^{+0.11}_{-0.17}$	$7.82^{+1.17}_{-1.27}$
						1250	5.24	52	2.5	0.1	17.3	$2.15^{+0.17}_{-0.06}$	$4.76^{+0.75}_{-0.63}$
						1251	4.60	69	2.5	0.1	20.1	$2.21^{+0.82}_{-0.87}$	$7.82^{+0.92}_{-0.92}$
						1252	3.64	68	2.5	0.1	15.7	$2.29^{+0.83}_{-0.87}$	$6.07^{+0.93}_{-0.92}$
						1253	4.48	68	2.5	0.1	19.3	$2.26^{+0.08}_{-0.07}$	$8.62^{+0.93}_{-0.92}$
MRK 509	3.12	0.0344	7.84	68	1,2,3,4,5	161	2.97	30	2.5	0.1	1.3	$1.63^{+0.15}_{-0.13}$	$6.41^{+1.14}_{-1.15}$
						250	3.84	43	2.5	0.1	2.4	$1.72^{+0.15}_{-0.15}$	<3.04
						1073	3.67	85	2.5	0.1	4.6	1.69 ± 0.03	<2.73
						1074	3.70	46	2.5	0.1	2.5	$1.74^{+0.09}_{-0.09}$	<0.59
MCG -6-30-15	3.08	0.0077	5.84	0.67	3,8	1168	4.26	69	2.5	0.1	4.4	$1.71^{+0.08}_{-0.08}$	<0.72
						108A	2.62	43	2.5	0.1	168.0	$2.01^{+0.19}_{-0.05}$	<0.69
						108B	3.60	55	2.5	0.1	295.3	$2.50^{+0.08}_{-0.32}$	<1.56
						301	4.11	84	2.5	0.1	514.9	2.47 ± 0.05	7.30 ± 1.14
						302	4.53	127	2.5	0.1	858.1	$2.28^{+0.06}_{-0.04}$	6.77 ± 0.90
						303	4.01	125	2.5	0.1	747.6	$2.17^{+0.09}_{-0.09}$	± 0.70
MCG +8-11-11	2.36	0.0205	7.18	15	3	794	4.52	38	2.5	0.1	11.6	$1.64^{+0.09}_{-0.07}$	$1.37^{+0.80}_{-0.87}$
NGC 7314	2.16	0.0048	6.67	4.6	12	256	3.93	43	2.5	0.1	36.9	2.12 ± 0.09	<1.84
						1172	1.54	82	2.5	0.1	27.5	$1.94^{+0.14}_{-0.14}$	$2.68^{+1.25}_{-1.27}$
AKN 120	2.14	0.0323	8.14	134	1,2,3,4,5	679	3.76	112	2.5	0.1	3.1	$1.97^{+0.07}_{-0.07}$	$3.84^{+1.85}_{-1.85}$
MRK 279	2.13	0.0305	7.79	60	1,2,3,5	1087	2.60	59	5.0	0.1	2.6	$1.91^{+0.06}_{-0.06}$	$1.03^{+0.73}_{-0.99}$
						1088	2.43	59	5.0	0.1	2.4	$1.75^{+0.05}_{-0.05}$	<2.38
						1089	2.38	38	5.0	0.1	1.5	$2.03^{+0.08}_{-0.10}$	<2.07
NGC 3227	2.10	0.0039	7.39	24	1,2,3,4,5	447	2.03	64	5.0	0.1	0.5	$2.10^{+0.03}_{-0.15}$	$4.20^{+2.06}_{-2.00}$
						178	0.85	35	5.0	0.1	1.2	$1.61^{+0.20}_{-0.13}$	<2.14
MR 2251-178	2.10	0.0640	8.40	246	10	1279	3.64	106	5.0	0.1	16.1	1.92 ± 0.08	$1.85^{+2.75}_{-2.30}$
IRAS 05078+1626	2.08	0.0179	7.04	11	1	265	2.44	129	5.0	0.1	386.0	$2.10^{+0.04}_{-0.03}$	$7.84^{+2.75}_{-2.04}$
						1410	2.41	108	5.0	0.1	13.0	$1.78^{+0.10}_{-0.09}$	$2.89^{+2.08}_{-2.08}$
MRK 590	1.95	0.0264	7.37	23	1,2,4,5	82	0.72	39	8.0	0.1	83.9	$1.85^{+0.43}_{-0.35}$	$2.53^{+1.46}_{-1.45}$
						837	1.52	129	5.0	0.1	2.6	$2.30^{+0.37}_{-0.37}$	$5.21^{+4.66}_{-1.97}$
MRK 766	1.77	0.0129	5.92	0.82	3	999	0.56	108	5.0	0.1	135.8	$1.99^{+0.26}_{-0.26}$	$3.46^{+2.29}_{-1.46}$
						1000	1.13	95	8.0	0.1	135.8	$2.53^{+1.46}_{-1.45}$	<1.20
						1001	1.40	98	6.5	0.1	168.3	$2.13^{+0.11}_{-0.07}$	<2.77
						1002	1.74	95	5.0	0.1	202.7	$2.27^{+0.16}_{-0.11}$	$3.59^{+1.23}_{-1.46}$

Table 2. continued.

Sources	RXTE (cts/s)	z	$\langle\mathrm{Log}(M_{\mathrm{BH}}/M_\odot)\rangle$	$\langle T_{\mathrm{orb}}(10\,r_g)\rangle$ (ks)	Ref.	Rev. Num.	$F_{2-10\,\mathrm{keV}}$ (10^{-11} erg cm^{-2} s^{-1})	Obs. Duration (ks)	Δt (ks)	ΔE (keV)	FOM (10^{-11} erg cm^{-2} s^{-1})	Γ	N_{H} (10^{22} cm^{-2})
(1)	(2)	(3)	(4)	(5)	(6)	(7)	(8)	(9)	(10)	(11)	(12)	(13)	(14)
NGC 7469	1.69	0.0164	7.14	13	1, 2, 3, 4, 5	1003	1.48	98	5.5	0.1	177.9	$2.01^{+0.17}_{-0.15}$	<2.23
						1004	1.30	35	5.0	0.1	55.8	$2.10^{+0.15}_{-0.08}$	<5.06
						192B	2.66	23	5.0	0.1	4.6	$1.79^{+0.11}_{-0.15}$	<1.18
						192A	2.49	18	5.0	0.1	3.4	$1.88^{+0.09}_{-0.11}$	<3.97
						912	2.83	85	2.5	0.1	18.0	$1.92^{+0.05}_{-0.08}$	$1.55^{+1.18}_{-0.93}$
						913	2.93	79	2.5	0.1	17.3	$1.97^{+0.07}_{-0.08}$	2.24 ± 1.09
MCG -2-58-22	1.61	0.0469	8.00	99	1, 3	180	3.02	10	2.5	0.1	0.3	$1.68^{+0.28}_{-0.28}$	<4.04
NGC 526A	1.61	0.0191	6.98	9	1, 13	647	2.20	44	2.5	0.1	10.5	$1.61^{+0.05}_{-0.05}$	$2.56^{+1.30}_{-1.44}$
NGC 4051	1.49	0.0023	5.90	0.77	2, 3, 4	263	2.35	117	5.5	0.1	355.8	$2.20^{+0.05}_{-0.05}$	$2.86^{+1.07}_{-1.10}$
						541	0.56	50	6.0	0.2	36.2	$1.56^{+0.23}_{-0.27}$	<4.35
ESO 141-G055	1.37	0.0360	7.51	31	1	1435 A	2.82	20	5.0	0.1	1.8	$2.06^{+0.31}_{-0.31}$	<3.88
						1435 B	2.54	21	5.0	0.1	1.7	$2.15^{+0.23}_{-0.23}$	<5.42
UGC 3973	1.32	0.0222	7.74	54	1, 2, 4, 5	1436	2.31	41	5.0	0.1	3.0	$2.10^{+0.19}_{-0.24}$	<3.31
						1445	2.88	78	5.0	0.1	7.2	$1.94^{+0.06}_{-0.06}$	<0.78
						1247	2.33	21	5.0	0.1	0.9	$2.02^{+0.08}_{-0.08}$	<4.65
						1263	2.01	20	5.0	0.1	0.7	$1.64^{+0.16}_{-0.17}$	<3.17
						1332	1.84	20	5.0	0.1	0.7	$1.63^{+0.23}_{-0.23}$	<4.25
						1535	0.77	87	6.0	0.1	1.2	$1.70^{+0.29}_{-0.29}$	$5.87^{+3.32}_{-1.37}$
Fairall 9	1.25	0.0470	8.00	98	1, 2, 3, 4, 5	105	1.16	29	5.0	0.1	0.3	$1.73^{+0.19}_{-0.29}$	<5.00
ESO 198-G024	1.21	0.0455	8.38	235	1, 9	207	1.30	31	5.0	0.1	0.2	$1.84^{+0.16}_{-0.16}$	<3.43
MRK 110	1.17	0.0353	6.99	9.5	2, 3, 4, 5	1128	1.02	122	6.0	0.1	0.5	$1.75^{+0.15}_{-0.15}$	$1.83^{+1.78}_{-1.38}$
						904	2.80	47	2.5	0.1	13.8	1.87 ± 0.10	$1.79^{+1.30}_{-1.36}$
AKN 564	1.13	0.0247	6.24	1.7	3, 7	930	1.60	99	5.0	0.2	94.1	$2.50^{+0.11}_{-0.04}$	<1.28
NGC 7213	1.12	0.0058	8.04	107	1, 11	269	2.16	42	5.0	0.1	0.9	$1.69^{+0.06}_{-0.03}$	<0.85
ESO 511-G030	1.10	0.0224	8.66	448	6	1402	1.93	109	5.0	0.1	0.5	1.89 ± 0.08	$2.03^{+1.15}_{-1.07}$
MRK 704	1.06	0.0292	7.55	35	1	1074	0.99	21	5.0	0.2	0.6	$1.88^{+0.40}_{-0.40}$	$6.58^{+5.44}_{-2.47}$
NGC 4593	1.05	0.0047	6.91	7.9	1, 2, 3, 5	1630	1.07	98	5.5	0.1	3.0	$1.87^{+0.15}_{-0.17}$	<3.57
						465	4.00	76	2.5	0.1	38.5	$1.84^{+0.06}_{-0.03}$	$1.21^{+0.91}_{-0.93}$

Columns: (2) RXTE count rate; (5) estimated Keplerian orbital period at $r = 10\,r_g$; (6) references for the mass estimates.; (10) and (11) chosen time and energy resolutions for the excess map analysis; (12) *FOM* value (see Sect. 4); References: (1) Wang & Zhang (2007); (2) Peterson et al. (2004); (3) Bian & Zhao (2003); (4) Kaspi et al. (2000); (5) Ho (1998); (6) Winter et al. (2008); (7) Botte et al. (2004); (8) Vaughan et al. (2003); (9) Rokaki & Boisson (1999); (10) Brunner et al. (1997); (11) Nelson & Whittle (1995); (12) Padovani & Rafanelli (1988); (13) Wandel & Mushotzky (1986).

Table 3. Gaussian components included in the best-fit models to the 4–9 keV time-averaged spectra, obtained assuming a "power-law + cold absorption" as the continuum model. The errors are computed at 90% confidence level.

Source (rev. number)	Red				Core				Blue				Absorption			
(1)	E (2)	σ (3)	EW (4)	I (5)	E (6)	σ (7)	EW (8)	I (9)	E (10)	σ (11)	EW (12)	I (13)	E (14)	σ (15)	EW (16)	I (17)
IC 4329a (rev. 210)					$6.43^{+0.04}_{-0.03}$	<0.1	59^{+24}_{-19}	9.9								
IC 4329a (rev. 670)	$6.34^{+0.10}_{-0.31}$	$0.34^{+0.17}_{-0.12}$	52^{+19}_{-30}	5.9	6.40 ± 0.01	0.06 ± 0.03	52^{+21}_{-15}	5.7	$6.97^{+0.06}_{-0.08}$	$0.10^{+0.08}_{-0.07}$	17^{+17}_{-9}	1.5	$7.67^{+0.05}_{-0.02}$	<0.11	-11^{+4}_{-6}	-0.8
MCG-5-23-16 (rev. 363)	$6.19^{+0.16}_{-0.20}$	$0.37^{+0.20}_{-0.24}$	74^{+33}_{-37}	7.6	$6.42^{+0.02}_{-0.01}$	<0.1	66^{+36}_{-15}	6.2								
MCG-5-23-16 (rev. 1099)	$6.35^{+0.05}_{-0.06}$	$0.34^{+0.07}_{-0.06}$	90^{+15}_{-17}	9.6	6.41 ± 0.01	<0.06	41^{+11}_{-9}	4.4	7.02 ± 0.03	<0.09	13^{+6}_{-5}	1.1				
NGC 3783 (rev. 372)	$6.09^{+0.32}_{-0.06}$	$0.46^{+0.65}_{-0.05}$	45^{+22}_{-18}	3.4	$6.40^{+0.02}_{-0.02}$	$0.06^{+0.04}_{-0.03}$	95^{+14}_{-9}	6.2	$7.01^{+0.03}_{-0.15}$	<0.16	26^{+8}_{-9}	1.4	$6.67^{+0.25}_{-0.19}$	<0.47	-20 ± 7	-1.4
NGC 3783 (rev. 371)	$5.80^{+0.27}_{-0.20}$	$0.45^{+0.27}_{-0.18}$	66^{+45}_{-20}	3.5	6.39 ± 0.02	0.06 ± 0.02	137^{+12}_{-13}	6.4	6.98 ± 0.04	0.10 ± 0.04	59 ± 14	2.3	7.68 ± 0.10	$0.20^{+0.18}_{-0.09}$	-57 ± 18	-2.5
NGC 3783 (rev. 193)	6.21 ± 0.05	<0.13	<28	1.0	6.38 ± 0.01	$0.05^{+0.15}_{-0.04}$	109^{+10}_{-11}	6.8	7.00 ± 0.04	<0.02	26 ± 9	1.4	6.60 ± 0.04	<0.16	-16^{+7}_{-39}	-1.1
NGC 5548 (rev. 191)					6.39 ± 0.02	$0.09^{+0.03}_{-0.02}$	79^{+9}_{-10}	3.3								
NGC 5548 (rev. 290)					6.40 ± 0.02	<0.06	74^{+15}_{-16}	2.5								
NGC 5548 (rev. 291)					6.37 ± 0.03	$0.06<0.11$	57^{+11}_{-13}	3.1								
NGC 3516 (rev. 245)	$6.29^{+0.08}_{-0.22}$	$0.22^{+0.11}_{-0.15}$	63^{+21}_{-30}	2.3	6.42 ± 0.01	<0.05	88^{+15}_{-14}	2.9								
NGC 3516 (rev. 352)	$6.40^{+0.11}_{-0.12}$	$0.62^{+0.08}_{-0.13}$	214^{+42}_{-41}	6.3	6.41 ± 0.01	0.07 ± 0.01	207 ± 15	5.2								
NGC 3516 (rev. 1250)	$5.98^{+0.07}_{-0.04}$	<0.17	19 ± 7	1.4	6.39 ± 0.02	$0.09^{+0.03}_{-0.02}$	88 ± 10	5.5					6.72 ± 0.03	<0.09	-22^{+7}_{-8}	-1.3
													$7.03^{+0.04}_{-0.03}$	<0.09	-27 ± 8	-1.3
NGC 3516 (rev. 1251)					$6.47^{+0.07}_{-0.03}$	$0.18^{+0.07}_{-0.04}$	221^{+126}_{-56}	10.9					$6.66^{+0.03}_{-0.05}$	0.08 ± 0.04	-69^{+51}_{-54}	-4.5
													7.04 ± 0.06	<0.08	-28^{+15}_{-82}	-1.3
NGC 3516 (rev. 1252)					6.39 ± 0.01	$0.10^{+0.02}_{-0.03}$	134^{+8}_{-15}	6.8					$6.77^{+0.04}_{-0.06}$	<0.12	-23^{+9}_{-9}	-1.1
													$7.07^{+0.02}_{-0.08}$	<0.08	-28 ± 8	-1.1
NGC 3516 (rev. 1253)					$6.46^{+0.04}_{-0.13}$	$0.14^{+0.07}_{-0.02}$	184^{+221}_{-36}	9.1					$6.66^{+0.08}_{-0.08}$	0.09 ± 0.08	-57^{+47}_{-107}	-3.4
													$7.08^{+0.03}_{-0.08}$	$0.01^{+0.09}_{-0.05}$	-27 ± 10	-1.2
MRK 509 (rev. 161)					6.38 ± 0.03	0.08 ± 0.05	76^{+16}_{-18}	2.6								
MRK 509 (rev. 250)					6.42 ± 0.03	$0.01^{+0.36}_{-0.01}$	30^{+17}_{-13}	1.4	$6.64^{+0.26}_{-0.14}$	$0.23^{+0.13}_{-0.15}$	48 ± 24	2.1				
MRK 509 (rev. 1073)					6.43 ± 0.02	0.12 ± 0.03	74 ± 10 eV	2.8	$7.02^{+0.06}_{-0.07}$	<0.17	24^{+10}_{-9}	0.8	$8.00^{+0.04}_{-0.02}$	<0.06	-20^{+8}_{-11}	-0.5
MRK 509 (rev. 1074)					$6.44^{+0.03}_{-0.04}$	$0.12^{+0.03}_{-0.05}$	76^{+12}_{-15}	2.8	$6.90^{+0.03}_{-0.05}$	<0.08	27 ± 10	0.9				
MRK 509 (rev. 1168)					6.44 ± 0.04	$0.10^{+0.07}_{-0.06}$	39 ± 12	1.8	$6.91^{+0.34}_{-0.24}$	$0.66^{+0.36}_{-0.39}$	120^{+44}_{-54}	4.7	$7.33^{+0.04}_{-0.02}$	<0.13	-26^{+11}_{-8}	-1.0
													8.50 ± 0.05	<0.12	-22^{+18}_{-13}	-0.6

Table 3. continued.

Source (rev. number) (1)	Red E (2)	Red σ (3)	Red EW (4)	Red I (5)	Core E (6)	Core σ (7)	Core EW (8)	Core I (9)	Blue E (10)	Blue σ (11)	Blue EW (12)	Blue I (13)	Absorption E (14)	Absorption σ (15)	Absorption EW (16)	Absorption I (17)
MCG-6-30-15 (rev. 108A)	$5.84^{+0.53}_{-1.37}$	$0.51^{+1.09}_{-0.47}$	98^{+639}_{-72}	3.2	$6.45^{+0.04}_{-0.10}$	$0.28^{+1.11}_{-0.10}$	162^{+73}_{-84}	4.1					6.67 ± 0.04	<0.11	-38^{+8}_{-205}	-1.1
MCG-6-30-15 (rev. 108B)					6.38 ± 0.02	<0.09	57 ± 10	2.5								
MCG-6-30-15 (rev. 301)					6.43 ± 0.04	0.25 ± 0.05	112^{+15}_{-16}	5.3								
MCG-6-30-15 (rev. 302)	$5.84^{+0.12}_{-0.48}$	$0.21^{+0.28}_{-0.61}$	25 ± 10	1.5	6.42 ± 0.03	$0.13^{+0.08}_{-0.03}$	67^{+8}_{-24}	3.3								
MCG-6-30-15 (rev. 303)	$5.37^{+0.25}_{-0.26}$	$0.71^{+0.22}_{-0.16}$	146^{+366}_{-12}	8.5	6.40 ± 0.03	0.21 ± 0.04	130^{+16}_{-50}	5.3	6.90 ± 0.04	<0.07 keV	13^{+8}_{-6}	0.5				
MCG +8-11-11 (rev. 794)					6.42 ± 0.01	$0.06^{+0.02}_{-0.05}$	119^{+11}_{-25}	5.9	$6.90^{+0.58}_{-0.51}$	$0.15^{+0.85}_{-0.73}$	43^{+18}_{-17}	1.9				
NGC 7314 (rev. 256)					6.40 ± 0.03	$0.10^{+0.05}_{-0.04}$	72 ± 14	3.1	$6.86^{+0.06}_{-0.07}$	$0.12^{+0.05}_{-0.06}$	52 ± 16	1.9				
NGC 7314 (rev. 1172)					6.42 ± 0.02	$0.10^{+0.02}_{-0.03}$	134^{+18}_{-19}	2.4								
ARK 120 (rev. 679)					$6.41^{+0.02}_{-0.07}$	$0.15^{+0.04}_{-0.07}$	127^{+9}_{-14}	4.8	$6.94^{+0.14}_{-0.31}$	$0.12^{+0.26}_{-0.05}$	42^{+9}_{-10}	1.4				
MRK 279 (rev. 1087)					6.43 ± 0.02	0.08 ± 0.03	96^{+15}_{-16}	2.6								
MRK 279 (rev. 1088)					$6.41^{+0.06}_{-0.07}$	$0.08^{+0.07}_{-0.02}$	99^{+23}_{-16}	2.5					$6.69^{+0.04}_{-0.05}$ $7.76^{+0.07}_{-0.08}$	<0.08 $0.12^{+0.15}_{-0.07}$	-22^{+8}_{-52} -55^{+18}_{-21}	-0.6 -1.0
MRK 279 (rev. 1089)					6.41 ± 0.03	0.08 ± 0.04	113 ± 21	3.1								
MR 2251-178 (rev. 447)					$6.42^{+0.05}_{-0.06}$	0.10 ± 0.08	51^{+14}_{-15}	1.2								
NGC 3227 (rev. 178)					6.39 ± 0.01	0.05 ± 0.02	202^{+26}_{-22}	2.7								
NGC 3227 (rev. 1279)	$6.02^{+0.08}_{-0.05}$	<0.18	27 ± 9	1.3	6.40 ± 0.01	0.06 ± 0.02	102^{+11}_{-10}	4.2								
IRAS 05078+1626 (rev. 1410)					$6.38^{+0.02}_{-0.03}$	<0.10	94^{+13}_{-33}	2.7	$6.66^{+0.09}_{-0.32}$	<0.35	17 ± 10	0.5				
MKN 590 (rev. 837)					6.44 ± 0.02	$0.07^{+0.03}_{-0.04}$	172^{+29}_{-31}	1.1	$7.02^{+0.09}_{-0.11}$	$0.07^{+0.2}_{-0.02}$	96^{+31}_{-37}	0.5				
MKN 766 (rev. 82)					$6.42^{+0.04}_{-0.03}$	<0.13	50^{+22}_{-29}	0.8	$6.80^{+0.12}_{-0.17}$	$0.22^{+0.17}_{-0.12}$	114^{+40}_{-39}	1.6				
MKN 766 (rev. 265)	$5.62^{+0.04}_{-0.03}$	<0.71	15^{+7}_{-6}	0.4	$6.38^{+0.05}_{-0.04}$	<0.10	15^{+20}_{-7}	0.4	$6.62^{+0.31}_{-0.05}$	$0.32^{+0.06}_{-0.14}$	159^{+17}_{-31}	3.4				
MKN 766 (rev. 999)	$5.98^{+0.19}_{-0.28}$	$0.42^{+0.15}_{-0.20}$	185^{+57}_{-58}	1.9	6.46 ± 0.03	<0.13	62^{+19}_{-55}	0.7	$6.70^{+0.10}_{-0.13}$	<0.40	43^{+20}_{-39}	0.4				
MKN 766 (rev. 1000)	$5.87^{+0.24}_{-0.29}$	$0.58^{+0.48}_{-0.09}$	165^{+49}_{-45}	2.2	6.40 ± 0.03	<0.28	47^{+21}_{-24}	0.6	$6.62^{+0.06}_{-0.09}$	$0.09^{+0.10}_{-0.05}$	56^{+17}_{-24}	0.7				

Table 3. continued.

Source (rev. number)	Red				Core				Blue				Absorption			
	E	σ	EW	I	E	σ	EW	I	E	σ	EW	I	E	σ	EW	I
(1)	(2)	(3)	(4)	(5)	(6)	(7)	(8)	(9)	(10)	(11)	(12)	(13)	(14)	(15)	(16)	(17)
MKN 766 (rev. 1001)	$5.86^{+0.05}_{-0.06}$	<0.12	19 ± 10	0.3	$6.41^{+0.15}_{-0.08}$	<0.28	64^{+18}_{-38}	0.9	$6.83^{+0.17}_{-0.19}$	$0.17^{+0.19}_{-0.11}$	99^{+23}_{-25}	1.2				
MKN 766 (rev. 1002)	$5.78^{+0.06}_{-0.05}$	<0.12	18 ± 9	0.4	$6.40^{+0.02}_{-0.03}$	<0.09	39^{+14}_{-13}	0.7	$6.77^{+0.06}_{-0.07}$	$0.20^{+0.07}_{-0.06}$	106^{+20}_{-22}	1.7				
MKN 766 (rev. 1003)	$5.93^{+0.03}_{-0.02}$	<0.20	20^{+12}_{-8}	0.3	$6.54^{+0.07}_{-0.06}$	0.26 ± 0.06	148 ± 25	2.0								
MKN 766 (rev. 1004)					$6.44^{+0.20}_{-0.12}$	$0.27^{+0.12}_{-0.20}$	139^{+115}_{-80}	1.9								
NGC 7469 (rev. 192A)					6.39 ± 0.02	<0.07	108^{+21}_{-22}	2.8								
NGC 7469 (rev. 192B)					6.41 ± 0.03	<0.14	90^{+17}_{-22}	2.4								
NGC 7469 (rev. 912)					6.40 ± 0.01	0.06 ± 0.02	95^{+10}_{-9}	2.8	7.00 ± 0.05	<0.14	21 ± 9	0.5				
NGC 7469 (rev. 913)					6.42 ± 0.02	0.08 ± 0.02	94^{+12}_{-11}	2.9								
MCG-2-58-22 (rev. 180)					$6.39^{+0.08}_{-0.09}$	$0.17^{+0.16}_{-0.08}$	107^{+40}_{-37}	3.6								
NGC 526A (rev. 263)					$6.38^{+0.03}_{-0.02}$	<0.09	34^{+14}_{-12}	1.0	$6.59^{+0.23}_{-0.14}$	$0.32^{+0.22}_{-0.13}$	82^{+30}_{-32}	2.2	$7.22^{+0.04}_{-0.05}$	<0.12	-19^{+10}_{-15}	−0.5
NGC 4051 (rev. 647)	$6.27^{+0.24}_{-0.20}$	$0.41^{+0.43}_{-0.22}$	68^{+26}_{-32}	1.9	6.39 ± 0.01	<0.07	68^{+11}_{-13}	1.8	$7.08^{+0.03}_{-0.04}$	<0.21	49^{+31}_{-27}	0.3	$7.08^{+0.06}_{-0.05}$	<0.18	-24^{+11}_{-12}	−0.5
NGC 4051 (rev. 541)	$6.13^{+0.11}_{-0.18}$	$0.65^{+0.16}_{-0.28}$	485^{+98}_{-95}	3.6	6.44 ± 0.02	$0.07^{+0.03}_{-0.04}$	196^{+28}_{-36}	1.5								
ESO 141-G055 (rev. 1435 A)					$6.35^{+0.11}_{-0.09}$	<0.27	70^{+31}_{-32}	2.0								
ESO 141-G055 (rev. 1435 B)					$6.54^{+0.19}_{-0.20}$	$0.39^{+0.20}_{-0.31}$	202^{+67}_{-70}	5.1								
ESO 141-G055 (rev. 1436)					6.35 ± 0.07	$0.17^{+0.08}_{-0.07}$	117^{+36}_{-33}	2.7	6.90 ± 0.03	<0.11	51^{+24}_{-22}	1.0				
ESO 141-G055 (rev. 1445)					$6.42^{+0.03}_{-0.02}$	<0.09	30^{+17}_{-13}	0.9	$6.62^{+0.20}_{-0.17}$	$0.45^{+0.26}_{-0.33}$	126^{+35}_{-59}	3.5	$8.31^{+0.03}_{-0.04}$	<0.11	-75 ± 20	−1.3

Table 3. continued.

Source (rev. number)	Red				Core				Blue				Absorption			
	E	σ	EW	I	E	σ	EW	I	E	σ	EW	I	E	σ	EW	I
(1)	(2)	(3)	(4)	(5)	(6)	(7)	(8)	(9)	(10)	(11)	(12)	(13)	(14)	(15)	(16)	(17)
UGC 3973 (rev. 1247)					6.44 ± 0.03	<0.08	69 ± 20	1.7								
UGC 3973 (rev. 1263)					6.42 ± 0.03	$0.04^{+0.08}_{-0.02}$	84^{+21}_{-23}	1.8								
UGC 3973 (rev. 1332)					6.38 ± 0.04	0.11 ± 0.04	122^{+31}_{-30}	2.5								
UGC 3973 (rev. 1535)					6.35 ± 0.01	$0.11^{+0.03}_{-0.02}$	284^{+26}_{-29}	3.1								
Fairall 9 (rev. 105)					6.40 ± 0.03	<0.11	126^{+24}_{-26}	1.7								
ESO 198-G24 (rev. 207)					6.51 ± 0.11	<0.36	60 ± 29	0.8								
ESO 198-G024 (rev. 1128)					6.41 ± 0.02	$0.07^{+0.02}_{-0.05}$	77^{+13}_{-14}	0.9					7.56 ± 0.13	<0.33	-49^{+23}_{-25}	-0.4
MKN 110 (rev. 904)					6.41 ± 0.04	<0.13	46 ± 13	1.4								
AKN 564 (rev. 930)					6.54 ± 0.10	$0.28^{+0.11}_{-0.08}$	94^{+24}_{-25}	1.2								
NGC 7213 (rev. 269)					6.40 ± 0.02	<0.08	79^{+17}_{-21}	1.8	$6.74^{+0.13}_{-0.16}$	$0.18^{+0.12}_{-0.10}$	59 ± 24	1.3				
ESO 511-G030 (rev. 1402)					6.39 ± 0.02	$0.12^{+0.04}_{-0.03}$	95 ± 13	2.0								
MRK 704 (rev. 1074)					$6.37^{+0.06}_{-0.07}$	$0.13^{+0.07}_{-0.06}$	159 ± 43	2.3								
MRK 704 (rev. 1630)					6.38 ± 0.02	0.11 ± 0.04	140^{+16}_{-22}	1.6								
NGC 4593 (rev. 465)					6.36 ± 0.01	<0.11	121 ± 10	5.2	$6.93^{+0.05}_{-0.006}$	$0.09^{+0.12}_{-0.08}$	37^{+10}_{-11}	1.4				

Notes: The rest-frame centroid energy (E) and width (σ) of the lines are given in units of keV, the equivalent width (EW) is in units of eV, the intensity (I) is in units of 10^{-5} ph s^{-1} cm^{-2}.

Appendix A: Notes on single sources

The aim of this section is to discuss and compare our results with previous studies, as many of the sources of our sample have been extensively investigated in literature. In general, the best fit models we used as templates for the simulations (see Table 3) are in good agreement with the ones derived by other authors from deeper broad X-ray band analysis. We mostly refer to the NOGR07 survey for broad Fe lines, as they analysed many of the observations treated in this paper. In the following we will focus on the most relevant sources.

IC 4329a: the addition of a broad and redshifted emission component to the best fit model is required at 99% confidence level (from intensity vs energy contour plots) during rev. 670. The detection of this line is confirmed by previous studies (Markowitz et al. 2006, NOGR07) on the same data set. However, its origin is controversial, being, most probably produced at $r > 50 \, r_g$, where relativistic effects cannot be robustly measured (see NOGR07). We registered significant flux variations within the energy band comprising this component, on time scales of ∼32 ks. We refer to De Marco et al. (2009) for a more comprehensive study of such emission feature.

On the contrary the redshifted component appears to be absent (in agreement with NOGR07 results) during the preceding observation (rev. 210). In this case, the non-detection of the line may be a consequence of the short exposure (∼10 ks). However, significant variability is detected in band B, pointing to the plausible presence of some kind of persisting, short-time scale variability phenomenon taking place in this source.

Detection of a blueshifted (∼0.1c) and constant flux absorption line is registered during rev. 670, in agreement with Markowitz et al. (2006) and NOGR07, possibly ascribable to FeXXVI.

MCG -5-23-16: this source has been deeply monitored via simultaneous observations with XMM-*Newton*, *Chandra* and Suzaku. This allowed accurate determination of the underlying continuum and detection of a relativistic Fe Kα line during rev. 1099. We confirm detection of a broad component during both rev. 363 and 1099, after restricting the analysis energy band to $E = 4$–9 keV. This line does not show significant variability, in good agreement with previous studies (Dewangan et al. 2003; Braito et al. 2007, NOGR07).

NGC 3783: we revealed a redshifted emission line in all the three observations (rev. 193, 371, 372), in agreement with published results (Blustin et al. 2002; Reeves et al. 2004; NOGR07). However, NOGR07 associate the broad component observed during rev. 193 to emission originated at $r > 50 \, r_g$. We also found signatures of a narrow absorption line at $E \sim 6.6$ keV during rev. 103 and 372, ascribed by Reeves et al. (2004) to a blend of FeXXIII, FeXXIV and FeXXV lines at the systemic velocity of the source. Reeves et al. observed that the line decreased its intensity between rev. 371 and rev. 372, indicating a variability time scale of ∼10^5 s for the highly ionized absorber. Although our technique does not test variability between different revolutions, we can nonetheless confirm these findings, as we do not have strong evidence for an absorption line detected during rev. 371. However, it is worth noting that the line is present during rev. 193, in good agreement with results of NOGR07.

An exhaustive temporal study of the spectral features in the 3 XMM-*Newton* observations of NGC 3783 has been published by Tombesi et al. (2007). Our analysis resembled the overall results of this paper.

NGC 3516: narrow, energy shifted emission components in the Fe K line profile were for the first time detected during a simultaneous *Chandra* and XMM-*Newton* (rev. 352) observation of NGC 3516 (Turner et al. 2002). Variability of the narrow redshifted emission feature at $E \sim 6.08$ keV (Bianchi et al. 2004) has been widely investigated by IMF04 for rev. 245 using the excess map technique, finding a variability confidence level of 97%. The pre-defined redshifted energy band we used for our analysis (band A, see Sect. 3.3) is broader than the energy band monitored by IMF04 (i.e. 5.8–6.2 keV), hence the light curve variations are smoothed out. However, restricting the energy band to the one considered in IMF04 we achieve the same variability confidence level (i.e. 97.1%).

In addition, different layers of absorbing gas were revealed during rev. 245 and 352 (Turner et al. 2005, NOGR07). Here we did not not account for these components as the narrow energy band in which we focus our analysis is not strongly affected by them. However, the technique we used to trace variability is nonetheless able to reveal high energy transient components of the absorbing gas. On the contrary, we observed two deep absorption lines in the average spectra of NGC 3516 during four consecutive revolutions (i.e. rev. 1250, 1251, 1252, 1253, covering the period 2006 Oct. 6–13), in the 6.7–7.1 keV regime (coincident with the C band), which can be associated to H-like and He-like species of Fe. These lines were ascribed by Turner et al. (2008) to a disk wind with outflowing velocities in the range 1000–2000 km s^{-1}. All these absorbing structures seem responsible for the significant variability revealed in band C during rev. 245, 1250, 1251 and 1252. We point out that the lack of variability during rev. 1253 is not due to statistical problems as the observation has approximately the same duration and flux as the previous three.

MRK 509: as pointed out by NOGR07, the statistical significance of the relativistic Fe Kα line during rev. 161 is comparable to the one obtained using a distant reflector model. Hence we adopted a simple, relatively narrow Gaussian template to fit the line. We further observed two absorption features during rev. 1073 and 1168. One of these ($E \sim 7.33$ keV) is also revealed in the synthesis spectrum (averaged out over all the five exposures) of Ponti et al. (2009), and its origin is ascribed to highly ionized outflowing ($v \sim 14\,000$ km s^{-1}) gas. On the contrary the high energy one ($E \sim 8.0$ keV) is also detected by Cappi et al. (2009) and Tombesi et al. (2009). We observed significant variability in band B during rev. 161 and 1168, in agreement with results obtained from the total rms spectrum analysis (Ponti et al. 2009). Moreover we found signatures of significant variability in Band A during rev. 161 and 1073.

MCG -6-30-15: in this particular case the relativistic Fe Kα line (e.g. Wilms et al. 2001) extends over the entire energy band where we focused our analysis. As the band is too narrow to obtain a good fit of the broad Fe line, the induced residual spectral bending can be modelled as due to continuum emission. Hence, as a consequence of the adopted technique and energy resolution (i.e. $\Delta E = 0.1$ keV), the mapping procedure is sensitive only to narrow spectral features above the broad line, and the corresponding flux measurements are robust against continuum modelling. The rms spectrum (with a time resolution of 6 ks) of the two observations carried out during rev. 108 shows a steep rise of variability at $E \sim 4.5$ keV with a peak at $E \sim 5.0$ keV (Ponti et al. 2004). We analysed the 2 observations with a finest time resolution (i.e. 2.5 ks) and found excess variability in all the three bands ($E \sim 5.4$–7.2 keV) during rev. 108B. The energy bands we analysed exclude the strong variability event observed in the rms spectrum.

The variations registered in the entire Fe K band during rev. 108B are most probably driven by the strong flare

observed in the continuum light curve (Ponti et al. 2004; Iwasawa & Miniutti 2004). Papadakis et al. (2005) studied the frequency-resolved spectra (Revnivtsev et al. 1999) of MCG -6-30-15 during rev. 108-303 and found that, although the broad Fe Kα line shows no significant variations on time scales less than ~1–2 days, some residuals between 5–7 keV are suggestive of small amplitude variations in a line-like feature. Moreover the drop observed in the spectra in the Fe Kα regime is less than the one expected from a constant line. Vaughan & Fabian (2004), using the flux-flux linear correlation (between soft band, 1–2 keV, and hard band, 3–10 keV) technique, deduced that flux variations are dominated by changes in the normalization of the power-law component. This is in agreement with our assumption in the Monte Carlo simulations, where we assume that only the power-law normalization varies, while the other components are constant. In addition there must be an additional component that varies little, and contributes more in the 3–10 keV band than in the 1–2 keV. The largest fractional contribution from this component occurs in the Fe K band, where it accounts for ~40% of the total flux. Once the variable continuum is subtracted from the total spectrum (see Sect. 3.3), the residuals should include only the nearly constant reflection component. Hence, the significant variations we observed in these residuals (during rev. 108B, 301 and 302) must be due to additional line-like features overlapping the broad Fe line profile, in agreement with deductions of Papadakis et al. (2005).

NGC 7314: a relativistic line or a distant reflector model can fit equally well the spectrum of this source during rev. 256 (NOGR07). For our analysis we assumed a simple model which accounts for the neutral and highly ionized Fe Kα emission lines. We found significant variations redward the neutral component during rev. 256. The detection of a narrow emission feature at $E \sim 5.8$ keV was also claimed by Yaqoob et al. (2003), in a *Chandra* observation taken 19–20 July 2002, and interpreted as redshifted Fe Kα emission. A hot spot origin of the line was ruled out by the authors because the estimated spot location resulted too large (i.e. $r > 132\ r_g$) to cause sufficient gravitational and Doppler redshift. In our spectrum, however, the feature is observed for about 20 ks (i.e. about half the duration of the observation). If produced in a spot – assuming a SMBH mass of $5 \times 10^6\ M_\odot$ (Padovani & Rafanelli 1988) – the emitting radius should be $r > 26\ r_g$ in order for the emission to correspond to less than one orbit (i.e. a spot and not an annulus). This estimated lower limit on the radius is still within the upper limit of $132\ r_g$.

It is worth noting that the target of the second XMM-*Newton* observation analysed in this paper (rev. 1172) is the cluster XMMUJ2235.3-2557, while NGC 7314 is observed off-axis, reducing the X-ray telescope's effective area.

NGC 3227: we detected a redshifted narrow emission feature during the longest observation (rev. 1279). Estimated parameters of this feature are in agreement with those derived in Markowitz et al. (2009) and double checked with MOS data. The energy of the feature results inconsistent with a Compton shoulder minimum energy (i.e. $E > 6.24$ keV). We did not find any significant evidence for variability in the Fe K band, in agreement with results of time resolved analysis in Markowitz et al. (2009).

MKN 766: a relativistic Fe K line was detected by NGO07 during rev. 82 and 265. To fit the curvature induced by this line we adopted a broad Gaussian component whose centroid energy falls in the energy range typical of a highly ionized Fe Kα and/or Fe Kβ line. Turner et al. (2006) reported on significant energy modulation (detected via excess map technique) during rev. 265, within $E \sim 6.1$–6.8 keV (band B), tracing a sinusoid of period ~150 ks. They associated this emission to orbiting material at an estimated distance of $r = 115\ r_g$ from the central BH. At such distance the increase in flux during the approaching phase of the orbital motion is not expected to be strong (e.g. Dovciak et al. 2004), in agreement with the results of our temporal analysis, which rules out the presence of any significant intensity modulation in the data. An extensive analysis of the entire set of observations (rev. 82, 265, 999-1004) available for this source, was carried out by Miller et al. (2006). They found variability in the low-ionization band ($E = 6.08$–6.48 keV), significant at 95%. This value is in agreement with the variability significance we estimated in Band B (which includes the low-ionization band of Miller et al.) during rev. 1004.

NGC 4051: we found evidence for broad emission at Fe K redshifted energies in both the observations (rev. 263 and 541). For what concerns rev. 263, our result is consistent with NOGR07. We did not detect significant variability in this source, in agreement with the rms spectrum (time resolution 2 ks) analysis carried out by Ponti et al. (2006).

AKN 564: *ASCA* observations of AKN 564 revealed an Fe Kα line origin in highly ionized material (dominated by H-like ions). The line results significantly broad (Turner et al. 2001). Variability measurements down to time scales of approximately a week constrained the bulk of the line to originate at small distances from the nucleus. Previous studies (Papadakis et al. 2007) on the ~100 ks XMM-*Newton* observation (rev. 930) revealed a Fe Kα line component slightly broader than the energy resolution of the EPIC-pn detector and rather weak (i.e. $EW \sim 70$ eV), in agreement with our best fit model (Table 3). However the line cannot be unambiguously ascribed to relativistic emission (see Papadakis et al. 2007; NOGR07). We detected significant variability in both band B and C where the only residuals visible in the map coincide with the Fe line. They seem to be absent at the very beginning of the observation; we rule out this to be a background subtraction effect, because the source signal results very high with respect to the background level (during the first 10 ks the background count rate in the 4–9 keV energy band is just 5% the source one).